

AN ABSTRACT OF THE THESIS OF

Peter Ferrero for the degree of Master of Science in Chemical Engineering presented on August 20, 2018.

Title: Steady-State Diffusion in a Spatially Varying Porous Medium

Abstract approved: _____

Brian D. Wood

Heterogeneous porous material represents a persistent challenge in the field of engineering. Microscale properties such as the porosity and microchannel tortuosity significantly control the macroscale transport characteristics of homogeneous porous medium. Additional complexity is introduced when these small-scale features vary in space. Examples of heterogeneous porous systems include artificial body tissues, groundwater flow across different soil types, and asymmetric membrane filtration systems. While these processes are ubiquitous in engineering applications, modeling a fully resolved porous material larger than a few millimeters is restricted by the availability of computational resources. Upscaling techniques such as the method of volume averaging use information from a small portion of the porous medium to derive parameter values to describe transport over the original large-scale system. This research aims to extend the method of volume averaging to modeling heterogeneous systems that contain significant porosity gradients. In particular, a new model is developed that incorporates information relating to the center of mass of the system to the overall transport properties of the heterogeneous porous material. This model is used to model mass transport within a variety of periodic and disordered porous media. The accuracy of the model is compared to previously described MVA models and the limitations and advantages of each model are detailed.

©Copyright by Peter Ferrero
August 20, 2018
All Rights Reserved

Steady-State Diffusion in a Spatially Varying Porous Medium

by

Peter Ferrero

A THESIS

submitted to

Oregon State University

in partial fulfillment of
the requirements for the
degree of

Master of Science

Presented August 20, 2018
Commencement June 2019

Master of Science thesis of Peter Ferrero presented on August 20, 2018.

APPROVED:

Major Professor, representing Chemical Engineering

Head of the School of Chemical, Biological, and Environmental Engineering

Dean of the Graduate School

I understand that my thesis will become part of the permanent collection of Oregon State University libraries. My signature below authorizes release of my thesis to any reader upon request.

Peter Ferrero, Author

ACKNOWLEDGEMENTS

To Dr. Brian D. Wood, I express my sincerest gratitude for always being available for a meeting to discuss my research. Your guidance has been invaluable in developing this body of work and your willingness to let me experiment with different numerical methods allowed me to develop as a researcher. Studying under you has broadened my view of the intricacies and subtleties found within mathematics. Your generosity will forever be remembered.

To the Chemical, Biological, and Environmental Engineering and Mathematics Departments I give my sincerest thanks. Particularly to Dr. Koretsky, Dr. Chang, Dr. Faridani, Dr. Bokil, and to Dr. Peszynska for their enlightening discussions that have certainly made me a better engineer and mathematician.

I thank Anita Hughes and Elisha Brackett for always being willing to provide assistance with all of my questions about graduate school.

My father and mother have always been exceptional role models with regards to the tenets of integrity, empathy, and assiduousness. I am indebted to them for instilling these values into me at an early age. Their support throughout the years has led me to where I am today. Thank you.

To my wife, Rachel, thank you for endeavoring these two past years to support us during graduate school. Her selflessness has made all of this possible. She is the light in my life.

Finally, I thank my dog, Flynn, for keeping my feet warm as I wrote this.

CONTRIBUTION OF AUTHORS

Thank you, Dr. Stephen Whitaker, for reviewing our work on developing the volume averaged model with the center of mass correction for porous mediums with gradient porosities. Your edits on the manuscript were also greatly appreciated.

TABLE OF CONTENTS

	<u>Page</u>
1 Introduction	1
2 Steady-State Diffusion in a Spatially Varying Porous Medium	6
2.1 Abstract	6
2.2 Introduction	7
2.3 Steady Diffusion in a Heterogeneous Porous Medium	9
2.3.1 Microscale balances	9
2.3.2 Averaging	10
2.3.3 The Closure Problem	15
2.3.4 Models with Increasing Order of Corrections	18
2.4 The Weighting Function	20
2.5 Case 1: Homogenous Periodic Media	22
2.6 Case 2 and 3: Steady Diffusion in a Spatially Varying Quasi-Periodic Porous Medium	26
2.6.1 Case 2	26
2.6.2 Case 3	29
2.7 Case 4: Steady Diffusion in a Spatially Varying Disordered Porous Medium	30
2.8 Convergence of the Taylor Series Approximation for the Average Flux	33
2.9 Conclusions	35
2.10 Simulation Files and Data	37
3 General Conclusions	38
Bibliography	39
Appendices	44
A Approximating the Average Molar Flux	45
B Analysis of Source Terms	50
C Convergence Analysis	53

LIST OF FIGURES

Figure	Page	
1.1	Volume averaging replaces a complex multiphase porous diffusion model with an equivalent single-phase model. The complicated geometry information of the original model is contained within the effective diffusivity tensor, \mathbf{D}_{eff} . Adapted from [1].	3
2.1	The relationship among the position vector, \mathbf{r} , the centroid, \mathbf{x} , and the displacement vector, \mathbf{y} within an averaging volume, \mathcal{V}	11
2.2	The discontinuous boxcar (left), mollified boxcar (middle), and mollified triangle weighting functions (right).	21
2.3	Case 1: a periodic domain averaged using a mollified triangle function (illustrated above the region to which it is applied) with a width of two periods. The grayed regions represent two different averaging volumes (with centroids located at x_1 and x'_1 , respectively). Note that the average is a continuous function, defined for all values of x_1	23
2.4	The effective diffusivity tensor, averaged concentration profiles, and relative errors of Case 1 (left column, top to bottom) and the porosity, x -component and x -derivative of the first moment vector (right column, top to bottom). . . .	25
2.5	The domains for the Case 2: gradually varying porosity (left) and Case 3: discontinuous porosity (right).	26
2.6	The effective diffusivity tensor, averaged concentration profiles, and relative errors of Case 2 (left column, top to bottom) and the porosity, x -component and x -derivative of the first moment vector (right column, top to bottom). . . .	27
2.7	The effective diffusivity tensor, averaged concentration profiles, and relative errors of Case 3 (left column, top to bottom) and the porosity, x -component and x -derivative of the first moment vector (right column, top to bottom) . . .	28
2.8	Case 4: a disordered porous medium with a 0.5 jump change in porosity. . . .	30
2.9	The xx -component of the effective diffusivity tensor, averaged concentration profiles, and relative errors of Case 4 (left column, top to bottom) and the porosity, x -component and x -derivative of the first moment vector (right column, top to bottom).	31
2.10	The Taylor series average flux approximation for Case 1 (top-left), Case 2 (top-right), Case 3 (bottom-left), and Case 4 (bottom-right).	33

LIST OF TABLES

<u>Table</u>		<u>Page</u>
2.1	The parameters used for Case 1.	24

LIST OF APPENDIX FIGURES

<u>Figure</u>	<u>Page</u>
A.1 The boxcar function (top-right) and the Taylor series approximated average flux for the Case 1 (top-left), the effective diffusivity coefficient (bottom-left) and the concentration profile (bottom-right) using a boxcar weighting function.	46
A.2 The mollified boxcar function (top-right) and the Taylor series approximated average flux for the Case 1 (top-left), Case 2 (bottom-left) and Case 4 (bottom-right) using a mollified boxcar weighting function.	47
A.3 The effective diffusion coefficient (left column) and average concentration profile (right column) for Case 1, Case 2, and Case 4 (top to bottom row) for the mollified boxcar function.	48
B.1 The first moment source term for Case 1 (top-left), Case 2 (top-right), Case 3 (bottom-left), and Case 4 (bottom-right).	51

LIST OF APPENDIX TABLES

<u>Table</u>		<u>Page</u>
C.1	The global convergence order, P_G , global GCI and average element size, \bar{h} for the DNS solution, closure problem, and upscaled equations for Case 1	53
C.2	The global convergence order, P_G , global GCI and average element size, \bar{h} for the DNS solution, closure problem, and upscaled equations for Case 2	53
C.3	The global convergence order, P_G , global GCI and average element size, \bar{h} for the DNS solution, closure problem, and upscaled equations for Case 3	54
C.4	The global convergence order, P_G , global GCI and average element size, \bar{h} for the DNS solution, closure problem, and upscaled equations for Case 4.	54

Chapter 1: Introduction

Porous materials are ubiquitous in nature and engineering. These multiphase materials often contain a skeletal solid matrix phase interlaced with fluid filled pores. Even dense materials such as glass and metal alloys may contain small pores within the solid matrix even though such materials are usually not classified as being porous [2, 3]. The morphology of the solid phase controls the transport characteristics of a porous material. For example, pores may form complicated interconnected networks that tend to inhibit the flow of solutes through a porous medium. These networks are defined by the diameter of the pore channels, the degree of straightness of these channels, and the interaction of a solute with the solid matrix to name a few. In addition to microscopic features, larger structures such as fractures and overall solid phase composition can significantly alter the flow of fluids through a porous material. While a mathematical model incorporating all of these effects may be derived, the act of solving these equations on a domain size relevant to engineering applications is challenging.

In modeling a porous material, two approaches are typically pursued: 1) small, highly detailed models fully resolved at the microchannel level and 2) macroscale models that implicit contain microscale information. While explicit, detailed models are highly accurate, only very small porous domains on the order of centimeters may be solved using such methods. This is because the geometry of such models is exceedingly complex, requiring three-dimensional models of the individual microchannels within the material. To accurately solve such a model with a finite element method, a very fine mesh must be used to resolve the pore network which may require millions of nodes. As a result, the amount of memory required to store the mesh and the matrices representing the model equations is extremely large and does not scale well as the size of the porous domain being modeled is increased. Furthermore, discretizing the governing differential equations results in extremely large systems of equations that usually require expensive iterative methods to solve. The cost is especially steep for

the case of transient and nonlinear transport equations which require many steps to solve. While sophisticated high performance computational systems exist to solve these types of models for more physically relevant domain sizes, most research groups do not have access to such resources. Computational fluid dynamics has been used to develop a highly resolved model of the fouling of a porous membrane by Blue Indigo dye [4]. The model was able to predict the fouling pattern of the membrane filter at various feed velocities. Another approach utilizes the extended Nernst-Planck equations which model solute transport through nanomembranes [5]. This approach accounts for diffusion, electromigration, and convection of charged particles due to concentration, electrical potential and pressure gradients across the membrane. Additionally, the interactions of the solute ions with the membrane matrix were accounted for using the nonlinear Poisson-Boltzmann equation. The solutions to this model were shown to agree well with experimental results for a range of solutions containing single salts, mixed electrolytes, and mixed solutes.

An alternative is to implicitly model the microscopic features of the porous material. This allows for the porous medium to be represented as a macroscale continuous material without explicitly modeling the complicated microchannel network. Typically, the effects of the microchannels are represented by parameter coefficients in the governing differential equation. A classic example of such a model is Darcy's law which typically models groundwater flow [6]. Darcy's law encompasses the effect of the porosity of the microchannels in the porous medium and the degree of connectedness of the pores through the use of a permeability coefficient. Because Darcy's law is applied to a macroscale domain, none of the geometric complexity of the microchannels is needed to be resolved by a mesh. This decreases the required amount of computational resources to solve the implicit model at the expense of model accuracy. Furthermore, the accuracy of Darcy's law relies on the assumption that the porous material is uniform and that no preferential flow pathways exist within the microchannel network such as a fracture. Darcy's law also is deficient at modeling heterogeneous materials such as porous mediums with large gradients in porosity.

In the past 60 years, many new heterogeneous porous media models have been developed.

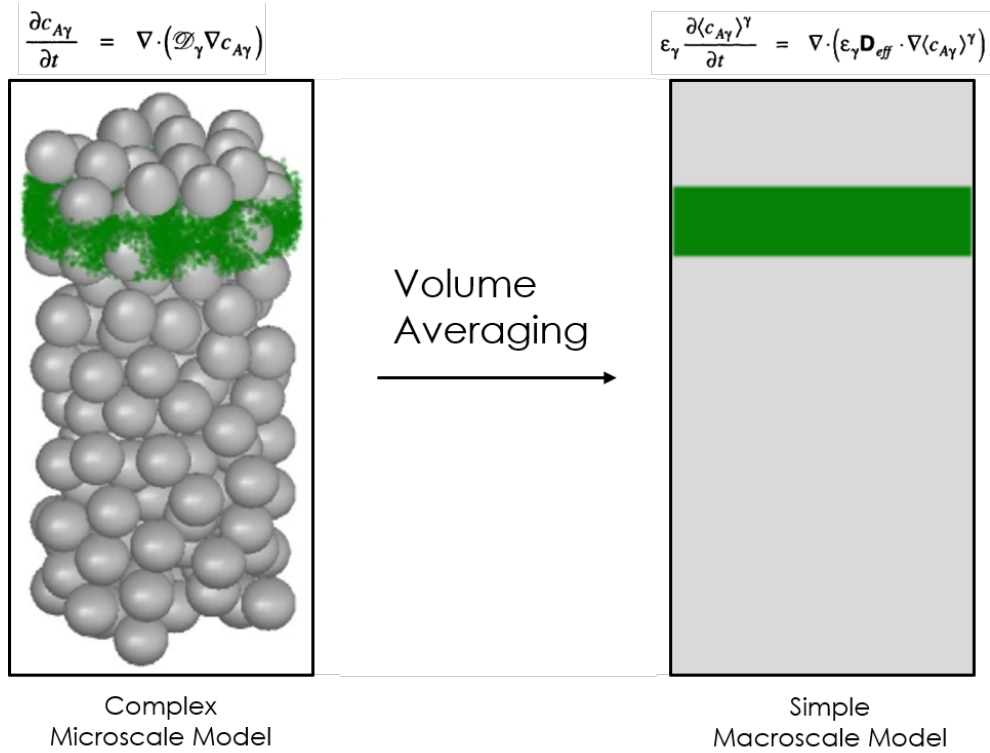


Figure 1.1: Volume averaging replaces a complex multiphase porous diffusion model with an equivalent single-phase model. The complicated geometry information of the original model is contained within the effective diffusivity tensor, \mathbf{D}_{eff} . Adapted from [1].

The equivalent continuum model is an example of an early implicit model which partitions the heterogeneities within porous material into smaller continuous domains and then solves for the resulting macroscale hydraulic properties for each subdomain [7, 8]. Another example is the dual-porosity model which divides the porous system into two components: the fractures and the solid matrix [9, 10]. Additionally, two sets of parameters are used to describe the transport within the fractures and the solid matrix with a coupling term that describes the diffusion of solutes between the two systems. This model was later generalized by the multiple interacting continua model which creates nested subdomains to model the hydraulic characteristics of flow through the fractured material as a function of the distance from the fracture [11]. The dual-permeability model is similar to the dual-porosity model except that it addresses the main limitation of the dual-porosity model by accounting for both diffusion *and* advection between the fractures and solid matrix [12, 13].

The method of volume averaging (MVA) [14] combines the best features of these two approaches. In this approach, an averaging operator is applied to the microscale governing differential equations for the fluid and solid phase. This produces a single new upscaled governing equation that is valid over both the fluid and solid fractions of the porous material. In effect, volume averaging replaces the original multiphase domain with a simple single-phase model. The geometrical complexities of the original domain are folded into the effective parameters produced during the averaging process. In developing the upscaled averaged equation, the microscale concentration is decomposed into an average and deviation component much like the Reynolds-averaged Navier-Stokes equations. To close the problem, a model for the deviation component must be created. This model is solved using a highly detailed representative elementary volume (REV) that captures the essential microscale information of the porous material. The solution of this closure model is used to calculate the effective hydraulic parameters that were produced during the upscaling process. Thus, the upscaled equation represents the implicit portion of the model and the closure problem solved over the REV contains the highly detailed explicit model.

This approach is successful because the REV is typically much smaller in size compared to the original porous material which saves computational resources. Due to this, the quality of the solution directly depends on the proper selection of the REV. In volume averaging, REVs are typically developed for disordered and periodic porous materials. While porous materials occurring in nature typically possess regions of random porous networks interspersed with ordered regions, a disordered media assumes that the porous network is completely random or statistically stationary. For a REV to be statistically stationary, it is required that the REV represent the average configuration of the material over many separate realizations. In addition to this, the REV must be large so that averaged quantities such as porosity and concentration fields do not fluctuate significantly between separate realizations of the porous material. Conversely, periodic porous materials are comprised a unit cell that repeats at regular intervals in space. The averaged parameters tend to fluctuate periodically across the unit cell as a result of the highly structured nature of periodic porous materials. In this

scenario, the REV is typically one unit cell of the periodic material.

While modeling homogeneous porous materials using upscaling techniques such as MVA, multiple scales [15] and homogenization theory [16] has been extensively studied, adapting these methods to heterogeneous media remains a challenging problem. Porosity-graded membrane filters are an example of such a material and are increasingly being used in the food and pharmaceutical industries due to their resistance to fouling. Standard membrane filters with constant porosity typically only separate contaminants at the surface of the membrane leaving the filter matrix below the surface under-utilized. Consequently, surface blockage drastically decreases the performance of the filter. The porosity of graded filters instead decrease across the membrane which allows for different sized contaminants to be removed at different depths along the filter. This causes the entire filter media to be utilized which increases the filtration efficiency and also decreases the occurrence of complete pore blockage. These types of filters would find extensive applications in kidney dialysis [17], dairy and fruit juice processing [18], and biopharmaceutical products filtered from blood [19]. Further applications of modeling heterogeneous porous media include nuclear waste disposal performance evaluation [20] and water treatment within stratified aquifers [21, 22], and intercellular transport within cell cytoskeletons [23].

In this work, we seek to extend MVA to model such heterogeneous porous materials with significant porosity gradients. In particular, our model incorporates geometrical properties such as the porosity and first moment when solving the closure problem and calculating the effective diffusivity tensor. The accuracy this model is compared against two previously reported MVA models for four porosity cases. The trends in the results are explained by examining the convergence of the Taylor series approximation of the molar flux for each porosity case.

Chapter 2: Steady-State Diffusion in a Spatially Varying Porous Medium

2.1 Abstract

The objective of this paper is to derive an upscaled model that well-approximates the mass transport of a substance through a porous matrix possessing significant porosity gradients. The method of volume averaging (MVA) is used to develop a model incorporating the microscale first moment of the porous material to improve accuracy. The model is tested in four cases: (1) a periodic homogeneous medium, (2) a quasi-periodic heterogeneous medium with a gradual porosity change, (3) a quasi-periodic heterogeneous material with a discontinuous jump in porosity, and (4) a disordered heterogeneous porous medium with a discontinuous jump in the porosity. This model is shown to compare favorably to the direct numerical simulation (DNS) in all four cases. For heterogeneous materials, the success of the MVA models are found to depend heavily on the type of weighted average used for the averaging. To illustrate this, the results using mollified triangle and boxcar functions are presented. Notably, the more traditional boxcar weighting function produces unphysical negative values for the effective diffusivity tensor while the triangle function is observed to successfully simulate the heterogeneous material. The differences in the performance of the weighting functions is explained by checking the convergence of the Taylor series that approximates averaged molar flux through the porous medium. A particularly interesting (and previously unaddressed) feature of this work is that we illustrate that even for periodic systems more than one unit cell should be used for closure, of there is no sensible method to compute the average as the averaging domain translates through one period of the periodic structure.

This work seeks to both expand the utility of MVA to simulating transport in heterogenous porous material while also exploring the subtle differences in modeling periodic and disorder

porous media. These results provide valuable insight into both of these areas.

2.2 Introduction

Porous materials with significant gradients in porosity occur for a number of applications. Examples include graded electrodes in lithium-ion batteries, membrane filters [24, 25], oil recovery from fractured reservoirs, and many others [21, 22, 26, 27]. Because this problem has relevance to applications, it has received significant recent interest on the theoretical front [28, 25, 29, 30]. Both the geometry of and transport phenomena within porous materials possess multiple length and time scales. The pore-scale attributes of the material (e.g., geometry, pore-space interconnectivity, particle size, microchannel tortuosity, etc.) significantly affect the macroscale transport of quantities such as heat and mass within the porous medium as a whole. The advent of pore-scale models has greatly advanced the understanding of the relationship between the microscale and macroscale features and phenomena. However, in practice, these models are typically limited to domains no larger than a few centimeters due to the enormous amount of computational degrees of freedom required to directly model every microchannel within a porous material (especially in three-dimensions).

Various upscaling methods have been developed whose purpose is to capitalize on redundant information in the porous structure so that more compact macroscale models can be used to simulation processes within a porous material. The method of volume averaging (MVA) is one such method, and is adopted in this paper for upscaling purposes. Instead of solving the pore-scale transport equations for a fully resolved porous domain, MVA identifies a representative elementary volume (REV) which contains a sample of the pore-scale domain information that well-represents the entire porous material on average. Using the REV, values for macroscale parameters such as the effective diffusivity tensors may be calculated and used to model large-scale transport across the porous media. These effective parameters represent the link between the original pore-scale model and the final macroscale model derived from the averaging process.

Porous media is typically classified as being either spatially periodic or disordered (stochas-

tic). Periodic porous media consists of an array of repeating sub-elements that together comprises the overall periodic system. These materials possess attractive properties such as increased surface area for heat exchange and surface catalysis applications which increases process efficiency. Furthermore, since the material is highly structured, the pressure drop of fluids flowing through periodic porous media has been shown to be much smaller than in disordered porous materials, thus making these very energy efficient materials [31]. On the other hand, natural materials tend to be disordered; this, for simulating the transport phenomena in random packings or natural media, one must generate suitably-prepared realizations of the appropriate structure. MVA handles these two classes of porous materials similarly with one notable exception: the choice of the REV. For periodic material, the REV is typically chosen to be the unit cell of the periodic structure (although, we will re-address such choices in the material that follows). Choosing the REV for a disordered system is generally more difficult. Since the REV represents the average configuration of many realizations of the porous media, it is generally required that the REV is large enough such that the average properties of the medium are constant over these separate realizations [30]. However, it is also necessary that the statistics of the transport phenomena be considered because they are not always of the same scale as the underlying geometry of the media (e.g., this can be the case, for example, when there is turbulence in porous media).

In this work, we derive averaged macroscale transport equations for mass transport in quasi-periodic and disordered porous material with large gradients in the porosity. The paper both compliments and extends existing work by including new corrections for the spatially-evolving structure.

The paper is organized as follows. In Section 2.3, the macroscale averaged balance equations are derived using MVA. The properties of the three weighting functions used in this work are detailed in Section 2.4. The following three sections present the results for the case of a periodic homogeneous porous material (Section 2.5), a periodic porous material with a jump in the porosity of various smoothnesses (Section 2.6), and finally, the case of two-dimensional disordered porous media with a jump in the porosity (Section 2.7). Section 2.8, seeks to

explain the success of the various models used by comparing the convergence of the Taylor series approximation of the average flux for many of the cases studied. Finally, we conclude in Section 2.9 with a short summary of the primary results presented in this study.

2.3 Steady Diffusion in a Heterogeneous Porous Medium

2.3.1 Microscale balances

In the material that follows, we examine the upscaling of both a periodic medium and a disordered monodisperse medium. Both problems present some interesting complexities in upscaling despite the simplicity of the geometries. Although volume averaging is usually applied to the transient form of balance equations, here we will be considering only the *steady-state* solution of diffusion in a porous medium. This does not limit the analysis in any way, but it does allow us to focus on how the media structure influences transport properties without having to consider transient effects.

We represent the entire averaging volume as $\mathcal{V}(\mathbf{x})$ which is referenced by the location of its centroid, \mathbf{x} . Three distinct regions reside within the averaging volume for the two-phase system studied in this paper, namely, the γ -phase fluid region, denoted by $\mathcal{V}_\gamma(\mathbf{x})$, the κ -phase solid region, $\mathcal{V}_\kappa(\mathbf{x})$, and the set of γ - κ interfaces separating the two phases, $\mathcal{A}_{\gamma\kappa}(\mathbf{x})$. Formally, the averaging volume may be stated as a union of these three subdomains as given by

$$\mathcal{V}(\mathbf{x}) = \mathcal{V}_\gamma(\mathbf{x}) \cup \mathcal{A}_{\gamma\kappa}(\mathbf{x}) \cup \mathcal{V}_\kappa(\mathbf{x}) \quad (2.1)$$

Additionally, the boundary of the averaging volume forms a separate exterior interface denoted as $\mathcal{A}_e(\mathbf{x})$. This interface cuts across both γ - and κ -phase regions and is represented by

$$\mathcal{A}_e(\mathbf{x}) = \mathcal{A}_{\gamma e}(\mathbf{x}) \cup \mathcal{A}_{\kappa e}(\mathbf{x}) \quad (2.2)$$

where $\mathcal{A}_{\gamma e}(\mathbf{x})$ and $\mathcal{A}_{\kappa e}(\mathbf{x})$ represent the parts of the averaging volume boundary that intersects the γ - and κ -phase, respectively.

To start, we consider the following problem of pure (dilute) steady diffusion in a periodic material with finite scale for the period.

$$\nabla \cdot (\mathcal{D}_{A\gamma} \nabla c_{A\gamma}(\mathbf{r}, t)) = 0, \quad \text{for } \mathbf{r} \in \mathcal{V}_\gamma(\mathbf{x}) \quad (2.3)$$

$$B.C. 1 \quad -\mathbf{n}_{\gamma\kappa} \cdot (\mathcal{D}_{A\gamma} \nabla c_{A\gamma}(\mathbf{r}, t)) = 0, \quad \text{for } \mathbf{r} \in \mathcal{A}_{\gamma\kappa}(\mathbf{x}) \quad (2.4)$$

$$B.C. 2 \quad c_{A\gamma}(\mathbf{r}, t) = \mathcal{F}_\gamma(\mathbf{r}), \quad \text{for } \mathbf{r} \in \mathcal{A}_{\gamma c}(\mathbf{x}) \quad (2.5)$$

This set of equations is applied to the microscale and describes the process of mass transfer via diffusion (under the dilute solution approximation) everywhere in the fluid phase of the medium. Although the problem appears to be straightforward, the fluid-solid boundary can be quite complex, and this boundary subverts the otherwise simple structure of the problem. Thus, the description of the diffusion process over the entire domain \mathcal{V}_γ is a non-trivial problem.

The goal of volume averaging is to identify and capitalize on statistical or geometric *redundancies* in the information content of complex systems. Though we will not pursue concrete notions of information content in this work, the idea has enough intuitive appeal to convey the essential features of the upscaling process.

2.3.2 Averaging

The volume average can be defined in a number of ways; here, we adopt a distribution theory formulation because of its transparency for operations done on averages. Averages are identified with compact averaging domains (volumes) denoted $\mathcal{V}(\mathbf{x})$, where each averaging volume is identified uniquely by its centroid, \mathbf{x} . Typically, we assume that averaging volumes have a support domain with characteristic length scale r_0 , which can be represented by, for example, an integral scale of the correlation structure [32]. Any point in the field can be related to the centroid by the decomposition $\mathbf{r} = \mathbf{x} + \mathbf{y}$ (Fig. 2.1); this is similar to the approach used in the multiple-scale method of homogenization theory [?,]Chp. 7]Cioranescu2000. Note that

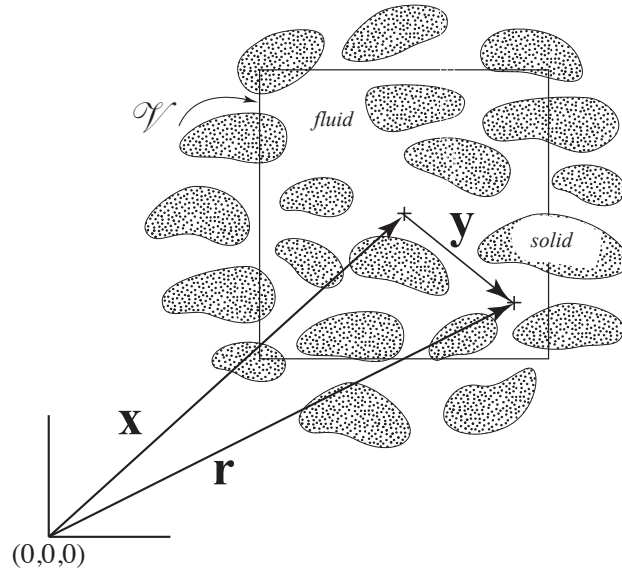


Figure 2.1: The relationship among the position vector, \mathbf{r} , the centroid, \mathbf{x} , and the displacement vector, \mathbf{y} within an averaging volume, \mathcal{V} .

we treat the vector \mathbf{y} as being embedded in an affine space, so that the displacement vector \mathbf{y} extends from the point \mathbf{x} to the point \mathbf{r} (or, conversely, $\mathbf{y}=\mathbf{r}-\mathbf{x}$).

The average of any field property $\psi(\mathbf{r})$ is specified by

$$\langle \psi \rangle_{\mathbf{x}} = \int_{\mathbf{r} \in \mathcal{V}(\mathbf{x})} \psi(\mathbf{r}) I_{\gamma}(\mathbf{r}) w(\mathbf{r} - \mathbf{x}) dV(\mathbf{r}) \quad (2.6)$$

Recalling the relationship $\mathbf{y} = \mathbf{r} - \mathbf{x}$ and the fact that the point \mathbf{x} is fixed, we can express this average equivalently as follows

$$\langle \psi \rangle_{\mathbf{x}} = \int_{\mathbf{y} \in \mathcal{V}(\mathbf{x})} \psi(\mathbf{x} + \mathbf{y}) I_{\gamma}(\mathbf{x} + \mathbf{y}) w(\mathbf{y}) dV(\mathbf{y}) \quad (2.7)$$

In both of these expressions, w is a compact C^{∞} weighting function, and I_{γ} is an indicator function defined by

$$I_{\gamma}(\mathbf{r}) = \begin{cases} 1, & \mathbf{r} \in \mathcal{V}_{\gamma}(\mathbf{x}) \\ 0, & \mathbf{r} \text{ otherwise} \end{cases} \quad (2.8)$$

As part of the upscaling process, we often need to exchange the operations of averaging with the spatial gradient. To do so, we adopt the use of the spatial averaging theorem [14, 33, 34]. Taking the gradient with respect to \mathbf{x} of both sides of Eq. (2.9), it is easy to develop the result

$$\langle \nabla \psi \rangle|_{\mathbf{x}} = \nabla \langle \psi \rangle|_{\mathbf{x}} + \int_{\mathbf{y} \in \mathcal{A}_{\gamma\kappa}(\mathbf{x})} \mathbf{n}_{\gamma\kappa} \psi(\mathbf{x} + \mathbf{y}) w(\mathbf{y}) dV(\mathbf{y}) \quad (2.9)$$

where $\mathbf{n}_{\gamma\kappa}$ is the vector pointing from the γ to κ -phase (Fig.2.1). Note that we have $\nabla_{\mathbf{x}} = \nabla_{\mathbf{y}} = \nabla_{\mathbf{r}}$ [35, 36], so that it is not necessary to explicitly indicate the variable for differentiation except for those cases where it is needed for clarity.

To proceed, we apply the averaging operations defined previously to both sides of the diffusion equation. Upon averaging and applying the spatial averaging theorem we find

$$\nabla \cdot (\mathcal{D}_{A\gamma} \langle \nabla c_{A\gamma} \rangle|_{\mathbf{x}}) + \int_{\mathbf{y} \in \mathcal{A}_{\gamma\kappa}(\mathbf{x})} \mathbf{n}_{\gamma\kappa} \cdot (\mathcal{D}_{A\gamma} \nabla c_{A\gamma}(\mathbf{x} + \mathbf{y})) w(\mathbf{y}) dA(\mathbf{y}) = 0 \quad (2.10)$$

Because of the boundary condition at the fluid-solid interface, this expression is immediately reducible to

$$\nabla \cdot (\mathcal{D}_{A\gamma} \langle \nabla c_{A\gamma} \rangle|_{\mathbf{x}}) = 0 \quad (2.11)$$

Applying the spatial averaging theorem a second time yields the result

$$\nabla \cdot \left[\mathcal{D}_{A\gamma} \nabla \langle c_{A\gamma} \rangle|_{\mathbf{x}} + \mathcal{D}_{A\gamma} \int_{\mathbf{y} \in \mathcal{A}_{\gamma\kappa}(\mathbf{x})} \mathbf{n}_{\gamma\kappa}(\mathbf{x} + \mathbf{y}) c_{A\gamma}(\mathbf{x} + \mathbf{y}) w(\mathbf{y}) dA(\mathbf{y}) \right] = 0 \quad (2.12)$$

To make further progress, it is useful to define the deviation concentration by the sum of the

mean plus a deviation

$$c_{A\gamma}(\mathbf{r}) = \langle c_{A\gamma} \rangle^\gamma |_{\mathbf{r}} + \tilde{c}_{A\gamma}(\mathbf{r}) \quad (2.13)$$

Note that this average is defined differently from those of Gray [33] and Bear [37], who define the deviations by subtracting the average concentration defined at the centroid, $\langle c_{A\gamma} \rangle^\gamma |_{\mathbf{x}}$.

In the remainder of the paper, we will no longer explicitly list the independent variables unless they are needed for clarity. Substituting this definition for the concentration decomposition into the averaged balance equation yields

$$\begin{aligned} \nabla \cdot \left[\mathcal{D}_{A\gamma} \nabla \langle c_{A\gamma} \rangle + \mathcal{D}_{A\gamma} \int_{\mathbf{y} \in \mathcal{A}_{\gamma\kappa}(\mathbf{x})} \mathbf{n}_{\gamma\kappa} \langle c_{A\gamma} \rangle^\gamma w(\mathbf{y}) dA(\mathbf{y}) \right. \\ \left. + \mathcal{D}_{A\gamma} \int_{\mathbf{y} \in \mathcal{A}_{\gamma\kappa}(\mathbf{x})} \mathbf{n}_{\gamma\kappa} \tilde{c}_{A\gamma} w(\mathbf{y}) dA(\mathbf{y}) \right] = 0 \end{aligned} \quad (2.14)$$

At this juncture, we can follow the example of [14, Chp. 1] which suggests expanding the average concentration as a Taylor series, and then adopts a sequence of *geometric theorems* to make further simplifications. Typically, the center of mass of the γ -phase is assumed to be constant. However, for a periodic averaging volume, the center of mass fluctuates across the course of one period as the location of the γ -phase changes with respect to the centroid of the averaging volume. Although the conventional order-of-magnitude arguments will not allow us to simplify the problem (because these arguments are essentially a form of *spatial stationarity* criteria for the geometric structure of the γ -phase), we can adopt an alternative approximate approach. To start, we require that the average concentration across the averaging volume can be well-approximated by a linear function. Thus, the Taylor series is explicitly approximated by

$$\langle c_{A\gamma} \rangle^\gamma |_{(\mathbf{x}+\mathbf{y})} = \langle c_{A\gamma} \rangle^\gamma |_{(\mathbf{x})} + \mathbf{y} \cdot \nabla \langle c_{A\gamma} \rangle^\gamma |_{\mathbf{x}} \quad (2.15)$$

In the material that follows, it will be convenient to define the following variables related to the spatial statistics of the indicator function. Recall that \mathbf{y} is an affine displacement

vector defined by the difference $\mathbf{y} = \mathbf{r} - \mathbf{x}$.

$$Y_0(\mathbf{r}; \mathbf{x}) = 1 \quad (2.16)$$

$$\mathbf{Y}_1(\mathbf{r}; \mathbf{x}) = (\mathbf{r} - \mathbf{x}) \quad (2.17)$$

$$\mathbf{Y}_2(\mathbf{r}; \mathbf{x}) = (\mathbf{r} - \mathbf{x}) \otimes (\mathbf{r} - \mathbf{x}) \quad (2.18)$$

$$(2.19)$$

or, alternatively

$$Y_0(\mathbf{y}; \mathbf{x}) = 1 \quad (2.20)$$

$$\mathbf{Y}_1(\mathbf{y}; \mathbf{x}) = \mathbf{y} \quad (2.21)$$

$$\mathbf{Y}_2(\mathbf{y}; \mathbf{x}) = \mathbf{y} \otimes \mathbf{y} \quad (2.22)$$

$$(2.23)$$

These definitions then allow us to define the (uncentered) spatial moments by [?]

$$M_0(\mathbf{x}) = \langle Y_0 \rangle |_{\mathbf{x}} = \int_{\mathbf{y} \in \mathcal{V}(\mathbf{x})} I_\gamma(\mathbf{x} + \mathbf{y}) w(\mathbf{y}) dV(\mathbf{y}) = \varepsilon_\gamma(\mathbf{x}) \quad (2.24)$$

$$\mathbf{M}_1(\mathbf{x}) = \langle \mathbf{Y}_1 \rangle |_{\mathbf{x}} = \int_{\mathbf{y} \in \mathcal{V}(\mathbf{x})} \mathbf{y} I_\gamma(\mathbf{x} + \mathbf{y}) w(\mathbf{y}) dV(\mathbf{y}) \quad (2.25)$$

$$\mathbf{M}_2(\mathbf{x}) = \langle \mathbf{Y}_2 \rangle |_{\mathbf{x}} = \int_{\mathbf{y} \in \mathcal{V}(\mathbf{x})} \mathbf{y} \otimes \mathbf{y} I_\gamma(\mathbf{x} + \mathbf{y}) w(\mathbf{y}) dV(\mathbf{y}) \quad (2.26)$$

Introducing the approximation given by Eq. (2.15) into Eq. (2.14), using the geometric theorems [14], and converting to the intrinsic average concentration yields the result

$$\begin{aligned} \nabla \cdot \left[\varepsilon_\gamma \mathcal{D}_{A\gamma} \nabla \langle c_{A\gamma} \rangle^\gamma - \underbrace{(\nabla \otimes \langle \mathbf{Y}_1 \rangle) \cdot \mathcal{D}_{A\gamma} \nabla \langle c_{A\gamma} \rangle^\gamma}_{\text{non-conventional correction term}} \right. \\ \left. + \mathcal{D}_{A\gamma} \int_{\mathbf{y} \in \mathcal{A}_{\gamma\kappa}(\mathbf{x})} \mathbf{n}_{\gamma\kappa} \tilde{c}_{A\gamma} w(\mathbf{y}) dA(\mathbf{y}) \right] = 0 \end{aligned} \quad (2.27)$$

This equation is the steady-state version of the result in [14, ?] with a first order correction arising from the geometrical structure of the porous medium. Physically, $\langle \mathbf{Y}_1 \rangle$ represents the center of mass of γ -phase within the averaging volume.

2.3.3 The Closure Problem

When upscaling microscale balance equations, equivalent effective parameters (in this case the effective diffusion coefficient) must be calculated by means of a closure problem. The closure problem accounts for the deviations in the microscale equations. Typically, a simple periodic REV is created that well represents any deviations generated by the geometrical features of the porous medium on the microscale. When deriving the closure problem, careful attention must be paid to the separation of the micro and macro length scales. The first step in deriving the closure problem for this example requires using the product rule to expand the divergence operator. Doing this yields the expanded version of Eq. (2.27)

$$\begin{aligned} \nabla \cdot (\mathcal{D}_{A\gamma} \nabla \langle c_{A\gamma} \rangle^\gamma) + \varepsilon_\gamma^{-1} \nabla \varepsilon_\gamma \cdot \mathcal{D}_{A\gamma} \nabla \langle c_{A\gamma} \rangle^\gamma \\ - \varepsilon_\gamma^{-1} (\nabla \cdot \nabla \otimes \langle \mathbf{Y}_1 \rangle) \cdot \mathcal{D}_{A\gamma} \nabla \langle c_{A\gamma} \rangle^\gamma \\ - \varepsilon_\gamma^{-1} \nabla \otimes \langle \mathbf{Y}_1 \rangle : \mathcal{D}_{A\gamma} \nabla \nabla \langle c_{A\gamma} \rangle \\ + \varepsilon_\gamma^{-1} \nabla \cdot \left[\mathcal{D}_{A\gamma} \int_{\mathbf{y} \in \mathcal{A}_{\gamma\kappa}(\mathbf{x})} \mathbf{n}_{\gamma\kappa} \tilde{c}_{A\gamma} w(\mathbf{y}) dA(\mathbf{y}) \right] = 0 \end{aligned} \quad (2.28)$$

The next step is to recall the decomposition given by Eq.(2.13); this suggests that an equation for the deviation balance can be found by subtracting the averaged equation (Eq. (2.28)) from

the point equation (Eq. (2.3)). The result of this operation is

$$\begin{aligned}
& \nabla \cdot (\mathcal{D}_{A\gamma} \nabla \tilde{c}_{A\gamma}) - \varepsilon_\gamma^{-1} \nabla \varepsilon_\gamma \cdot \mathcal{D}_{A\gamma} \nabla \langle c_{A\gamma} \rangle^\gamma \\
& + \varepsilon_\gamma^{-1} (\nabla \cdot \nabla \otimes \langle \mathbf{Y}_1 \rangle) \cdot \mathcal{D}_{A\gamma} \nabla \langle c_{A\gamma} \rangle^\gamma \\
& + \varepsilon_\gamma^{-1} \nabla \otimes \langle \mathbf{Y}_1 \rangle : \mathcal{D}_{A\gamma} \nabla \otimes \nabla \langle c_{A\gamma} \rangle^\gamma \\
& - \varepsilon_\gamma^{-1} \nabla \cdot \left[\mathcal{D}_{A\gamma} \int_{\mathbf{y} \in \mathcal{A}_{\gamma\kappa}(\mathbf{x})} \mathbf{n}_{\gamma\kappa} \tilde{c}_{A\gamma} w(\mathbf{y}) dA(\mathbf{y}) \right] = 0
\end{aligned} \tag{2.29}$$

$$B.C. 1 \quad -\mathbf{n}_{\gamma\kappa} \cdot (\mathcal{D}_{A\gamma} \nabla \tilde{c}_{A\gamma}) = \mathbf{n}_{\gamma\kappa} \cdot (\mathcal{D}_{A\gamma} \nabla \langle c_{A\gamma} \rangle^\gamma), \quad \text{for } \mathbf{x} \in \mathcal{A}_{\gamma\kappa} \tag{2.30}$$

$$B.C. 2 \quad c_{A\gamma\eta} = \mathcal{F}_\gamma(\mathbf{x}, t), \quad \text{for } \mathbf{x} \in \mathcal{A}_{\gamma e} \tag{2.31}$$

At this juncture, many of the remaining terms depend on the macroscale average concentrations. In order to fully decouple the microscale deviation concentration from the macroscale equation, constraints are typically defined that the REV must satisfy. Satisfying these constraints allows for the full decoupling of the deviation concentration from the average concentration. Generally, the effect of the nonlocal diffusion term is negligible in the closure problem [32], and it is neglected in further analysis (cf. [14]). While we allow for the gradient of the average concentration to be significant, we require that the term $\nabla \otimes \nabla \langle c_{A\gamma} \rangle^\gamma$ must be negligible; if it is not, then a third-order derivative term would arise in the macroscale equation, and this would create conceptual problems because third-order derivatives are not positive semi-definite operators. Making these assumptions and restrictions yields a final result of the form

$$\begin{aligned}
& \nabla \cdot (\mathcal{D}_{A\gamma} \nabla \tilde{c}_{A\gamma}) - \varepsilon_\gamma^{-1} \nabla \varepsilon_\gamma \cdot \mathcal{D}_{A\gamma} \nabla \langle c_{A\gamma} \rangle^\gamma \\
& + \varepsilon_\gamma^{-1} (\nabla \cdot \nabla \otimes \langle \mathbf{Y}_1 \rangle) \cdot \mathcal{D}_{A\gamma} \nabla \langle c_{A\gamma} \rangle^\gamma = 0
\end{aligned} \tag{2.32}$$

For the conditions explored here, it is clear that the volume diffusive source (involving the gradients of the porosity) are significant and cannot be neglected. Additionally, it is assumed that the second derivative of the center of mass is not negligible. This is based on the observation that the center of mass oscillates linearly as the centroid of the averaging volume moves across the periodic REV with sections of large local porosity variations as the averaging volume center crosses over the edges of squares within the periodic array. Thus, the deviations in the concentration may be characterized by the following governing differential equation

$$\nabla^2 \tilde{c}_{A\gamma} = \varepsilon_\gamma^{-1} \nabla \varepsilon_\gamma \cdot \nabla \langle c_{A\gamma} \rangle^\gamma - \varepsilon_\gamma^{-1} (\nabla \cdot \nabla \otimes \langle \mathbf{Y}_1 \rangle) \cdot \nabla \langle c_{A\gamma} \rangle^\gamma \quad (2.33)$$

At this juncture, we make the conventional arguments that the second boundary condition can be approximated, for the purposes of closure, by periodic conditions in the vertical and horizontal directions.

This leaves two source terms in the problem: one arising from $\nabla \langle c_{A\gamma} \rangle^\gamma$ in the balance equation, and one arising from $\nabla \langle c_{A\gamma} \rangle^\gamma$ in the boundary condition. Thus the integral solution for $\tilde{c}_{A\gamma}$ will involve Green's functions that generate both area and volume integrals of $\nabla \langle c_{A\gamma} \rangle^\gamma$. When localized [32], this will produce a solution with a single vector contracted with $\nabla \langle c_{A\gamma} \rangle^\gamma$. The localized form of the solution requires that a conventional separation of the length-scales be valid, i.e., $\ell \ll r_0 \ll L$, where ℓ is the characteristic length scale for the microscale, L is the characteristic length scale for the macroscale, and r_0 is a measure of the size of the support for the weighting function [32]. Thus, the localized closure variable takes the form

$$\tilde{c}_{A\gamma} = \mathbf{b}_\gamma(\mathbf{r}) \cdot \nabla \langle c_{A\gamma} \rangle^\gamma|_{\mathbf{r}} \quad (2.34)$$

In volume averaging, mapping functions such as $\mathbf{b}_{A\gamma}$ usually referred to as *closure variables*.

With this general form for $\tilde{c}_{A\gamma}$, we can develop a balance equation for the closure variable \mathbf{b}_γ . Substituting Eq. (2.34) into Eq. (2.33) and simplifying gives the following problem

$$\begin{aligned} \nabla^2 \mathbf{b}_\gamma &= \varepsilon_\gamma^{-1} \nabla \varepsilon_\gamma - \varepsilon_\gamma^{-1} \nabla \cdot \nabla \otimes \langle \mathbf{Y}_1 \rangle & (2.35) \\ \text{B.C. 1} \quad -\mathbf{n}_{\gamma\kappa} \cdot \nabla \mathbf{b}_\gamma &= \mathbf{n}_{\gamma\kappa}, & \text{for } \mathbf{x} \in \mathcal{A}_{\gamma\kappa} \\ \text{B.C. 2} \quad \mathbf{b}_\gamma(\mathbf{r} + \mathbf{l}) &= \mathbf{b}_\gamma(\mathbf{r}), & \text{for } \mathbf{x} \in \mathcal{A}_{\gamma\mathbf{e}} \end{aligned}$$

Substituting Eq. (2.34) into Eq. (2.27) yields

$$\begin{aligned} \nabla \cdot \left[\varepsilon_\gamma \mathcal{D}_{A\gamma} (\nabla \langle c_{A\gamma} \rangle^\gamma - \varepsilon_\gamma^{-1} \nabla \otimes \langle \mathbf{Y}_1 \rangle \cdot \nabla \langle c_{A\gamma} \rangle^\gamma \right. \\ \left. + \varepsilon_\gamma^{-1} \int_{\mathbf{y} \in \mathcal{A}_{\gamma\kappa}(\mathbf{x})} \mathbf{n}_{\gamma\kappa} \otimes \mathbf{b}_\gamma w(\mathbf{y}) dA(\mathbf{y}) \cdot \nabla \langle c_{A\gamma} \rangle^\gamma \right] = 0 \end{aligned} \quad (2.36)$$

Thus, the final closed problem can be put in the form

$$\nabla \cdot (\varepsilon_\gamma \mathbf{D}_{eff} \cdot \nabla \langle c_{A\gamma} \rangle^\gamma) = 0 \quad (2.37)$$

where the expression for the effective dispersion tensor is as follows

$$\mathbf{D}_{eff} = \mathcal{D}_{A\gamma} \left(\mathbf{I} + \varepsilon_\gamma^{-1} \int_{\mathbf{y} \in \mathcal{A}_{\gamma\kappa}(\mathbf{x})} \mathbf{n}_{\gamma\kappa} \otimes \mathbf{b}_\gamma w(\mathbf{y}) dA(\mathbf{y}) - \underbrace{\varepsilon_\gamma^{-1} \nabla \otimes \langle \mathbf{Y}_1 \rangle}_{\text{correction term}} \right) \quad (2.38)$$

2.3.4 Models with Increasing Order of Corrections

Three models are explored, each incorporating a successively higher order correction term to the diffusion tensor. These models are numbered 0, 1, and 2 which denotes the order of the term being maintained in the closure problem given by Equation (2.33). For example, the above model is labeled Model 2 since it neglects the second-order Taylor series term while including the zero- and first-order terms in the closure problem. The closure problems and

expressions of the effective diffusivity tensor of the three models are listed as follows

Model 0

$$\begin{aligned} \nabla^2 \mathbf{b}_\gamma &= 0 & (2.39) \\ \text{B.C. 1} \quad -\mathbf{n}_{\gamma\kappa} \cdot \nabla \mathbf{b}_\gamma &= \mathbf{n}_{\gamma\kappa}, & \text{for } \mathbf{x} \in \mathcal{A}_{\gamma\kappa} \\ \text{B.C. 2} \quad \mathbf{b}_\gamma(\mathbf{r} + \mathbf{l}) &= \mathbf{b}(\mathbf{r}), & \text{for } \mathbf{x} \in \mathcal{A}_{\gamma\mathbf{e}} \end{aligned}$$

$$\mathbf{D}_{eff} = \mathcal{D}_{A\gamma} \left(\mathbf{I} + \varepsilon_\gamma^{-1} \int_{\mathbf{y} \in \mathcal{A}_{\gamma\kappa}(\mathbf{x})} \mathbf{n}_{\gamma\kappa} \otimes \mathbf{b}_\gamma w(\mathbf{y}) dA(\mathbf{y}) \right) \quad (2.40)$$

Model 1

$$\begin{aligned} \nabla^2 \mathbf{b}_\gamma &= \varepsilon_\gamma^{-1} \nabla \varepsilon_\gamma & (2.41) \\ \text{B.C. 1} \quad -\mathbf{n}_{\gamma\kappa} \cdot \nabla \mathbf{b}_\gamma &= \mathbf{n}_{\gamma\kappa}, & \text{for } \mathbf{x} \in \mathcal{A}_{\gamma\kappa} \\ \text{B.C. 2} \quad \mathbf{b}_\gamma(\mathbf{r} + \mathbf{l}) &= \mathbf{b}(\mathbf{r}), & \text{for } \mathbf{x} \in \mathcal{A}_{\gamma\mathbf{e}} \end{aligned}$$

$$\mathbf{D}_{eff} = \mathcal{D}_{A\gamma} \left(\mathbf{I} + \varepsilon_\gamma^{-1} \int_{\mathbf{y} \in \mathcal{A}_{\gamma\kappa}(\mathbf{x})} \mathbf{n}_{\gamma\kappa} \otimes \mathbf{b}_\gamma w(\mathbf{y}) dA(\mathbf{y}) \right) \quad (2.42)$$

Model 2

$$\nabla^2 \mathbf{b}_\gamma = \varepsilon_\gamma^{-1} \nabla \varepsilon_\gamma - \varepsilon_\gamma^{-1} \nabla \cdot \nabla \otimes \langle \mathbf{Y}_1 \rangle \quad (2.43)$$

B.C. 1 $-\mathbf{n}_{\gamma\kappa} \cdot \nabla \mathbf{b}_\gamma = \mathbf{n}_{\gamma\kappa}, \quad \text{for } \mathbf{x} \in \mathcal{A}_{\gamma\kappa}$

B.C. 2 $\mathbf{b}_\gamma(\mathbf{r} + \mathbf{l}) = \mathbf{b}(\mathbf{r}), \quad \text{for } \mathbf{x} \in \mathcal{A}_{\gamma\mathbf{e}}$

$$\mathbf{D}_{eff} = \mathcal{D}_{A\gamma} \left(\mathbf{1} + \varepsilon_\gamma^{-1} \int_{\mathbf{y} \in \mathcal{A}_{\gamma\kappa}(\mathbf{x})} \mathbf{n}_{\gamma\kappa} \otimes \mathbf{b}_\gamma w(\mathbf{y}) dA(\mathbf{y}) - \underbrace{\varepsilon_\gamma^{-1} \nabla \otimes \langle \mathbf{Y}_1 \rangle}_{\text{correction term}} \right) \quad (2.44)$$

2.4 The Weighting Function

Typically, volume averaging uses a uniform weighting (boxcar) function when calculating averaged quantities such as the porosity (Fig. 2.2, left). However, the discontinuous boxcar function is limited in that the resulting averages do not necessarily possess continuous first derivatives. This presents a problem for closure problems of models 1 and 2 which require that the porosity and first moment possess continuous first and second derivatives.

The discontinuous boxcar function does not fulfill the requirements for smoothness because it is not a conventional distribution. Similarly, the indicator function $I_\gamma(\mathbf{r})$ is also discontinuous across the γ - κ interfaces and is also not a conventional distribution. As a result, the multiplication of the discontinuous boxcar and indicator function in Eq. (2.9) is not a defined operator according to conventional distribution theory, and this has the potential to create mathematical inconsistencies. Although there are new extensions of generalized functions that seek to address this scenario [?, ?], we opt here to remain within the confines of conventional distribution theory.

A simple method transform the discontinuous boxcar function into a conventional distribution is to convolve it with a mollifying function. The key characteristic of a mollifying function is that it is smooth or possesses derivatives of all orders. A common mollifier is the

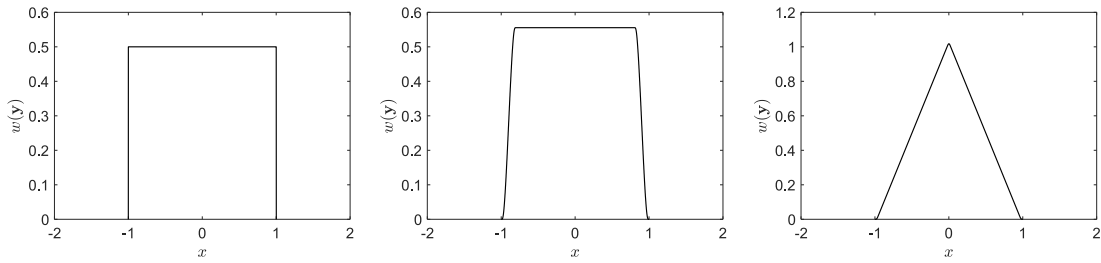


Figure 2.2: The discontinuous boxcar (left), mollified boxcar (middle), and mollified triangle weighting functions (right).

“bump function” defined by

$$m(x) = \begin{cases} \exp\left(-\frac{\epsilon_0^2}{\epsilon_0^2 - x^2}\right), & -\epsilon_0 < x < \epsilon_0 \\ 0, & \text{otherwise} \end{cases} \quad (2.45)$$

In addition to being infinitely differentiable, this function is compactly supported and as a result of this, the result of the convolution of any function with a mollifier is also a compactly supported smooth function.

Our initial simulations used a mollified boxcar function, defined by

$$w_{\square}(x) = \alpha_{\square} \int_{z=-\infty}^{z=\infty} B(x-z; x_-, x_+) m(z) dz = (B * m)(x) \quad (2.46)$$

where the boxcar function is given by

$$B(x-z; x_-, x_+) = H(x-x_-) - H(x-x_+) \quad (2.47)$$

Here, H is the Heaviside function, and α_{\square} is a constant that assures that the area under the weighting function is unity. The asterisk indicates convolution. The extension to multiple dimensions is made by multiplying appropriately shifted copies of the boxcar function B .

A particular feature of the mollified boxcar function is that it assigns nearly equal weighting over the entire averaging window (Fig. 2.2, middle). As a result, the mollified boxcar function acts nonlocally, and tends not to damp oscillations from the averaged quantities.

In the worst case scenario, these oscillations cause the effective diffusivity tensor to attain unphysical negative values; this creates a macroscale diffusion equation that is ill-posed (see the Appendix).

Conversely, previous studies have shown that triangle functions avoid many of these problems [30]. To explore this further, we adopt a mollified triangle function for weighting the volume averages (Fig. 2.2, right). The mollified triangle function serves as a filter for high frequency unphysical oscillations produced by the γ - κ interfaces intersecting the averaging window but is also a smooth function. Due to both of these attractive qualities, the main results of this work are produced using a mollified triangle function defined as follows

$$f_{\Delta}(x) = \begin{cases} 1 - \frac{|x|}{r_0 - \epsilon_0}, & -(r_0 - \epsilon_0) < x < (r_0 - \epsilon_0) \\ 0, & \text{otherwise} \end{cases} \quad (2.48)$$

$$w_{\Delta}(x) = \alpha_{\Delta}(f_{\Delta} * m)(x)$$

where $f_{\Delta}(x, y)$ is the (discontinuous derivative) triangle function, $w_{\Delta}(x, y)$ is the mollified triangle weighting function, and the integral of the weighting function is again forced to be unity through the normalization constant, α_{Δ} . The half-widths of the bump function and averaging window are represented by ϵ_0 and r_0 , respectively. Extensions to multiple dimensions are again done by multiplying appropriately shifted copies of the one-dimensional function. The mollified triangle was used as the weighting function for the cases 1-4 described below. For Cases 1-3 the weighting function was in one-dimension, whereas for Case 4 it was in two-dimensions.

2.5 Case 1: Homogenous Periodic Media

As a first examination of the effects of the corrections represented by model 0, model 1, and model 2, each of these models were implemented in a periodic array of squares (as illustrated in Fig. 2.3). In Fig. 2.3, the centroid of each square is located along the line $(x, 0)$; similarly, all averaging volumes are located this line. Note that any average property, then, is a continuous

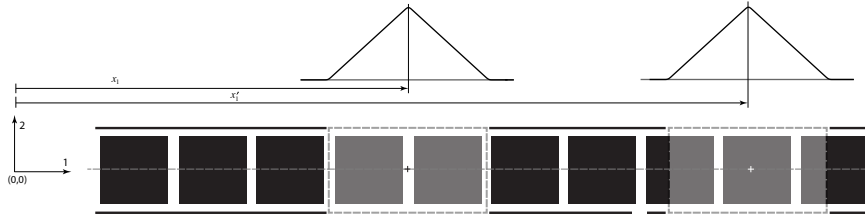


Figure 2.3: Case 1: a periodic domain averaged using a mollified triangle function (illustrated above the region to which it is applied) with a width of two periods. The grayed regions represent two different averaging volumes (with centroids located at x_1 and x'_1 , respectively). Note that the average is a continuous function, defined for all values of x_1 .

function of x (and, as defined here, does not depend upon y). The geometric properties of the system (porosity, gradient of porosity, center of mass, etc.) were calculated using the mollified triangle function defined over two periods in the x -direction. The triangle function was mollified using a bump function with a half-width, ϵ_0 equal to 2.5×10^{-5} (Fig. 2.4). The mollified triangle function is constant in the y -direction for reasons described shortly. Each period was $1[mm]$ in length in the x - and y -directions. Of special note is the handling of the domain edges in the x -direction. Since the γ -phase ends at the boundaries of the domain, the porosity and center of mass experience severe distortions as the averaging volume centroid approaches the domain boundary. For this work, the problem was handled by “padding” the domain with additional unit cells that were then truncated to eliminate those cells influenced by the boundary distortions.

The parameters for the simulations are summarized in Table 2.1. The DNS concentration profile was calculated by taking the intrinsic average of the solution of the microscale equations (Eqs. 2.3-2.5) solved over the entire macroscale domain. This average was calculated using the mollified triangle weighting function. Separately, the closure problem was solved across the microscale domain using Eq. (2.43). The periodic boundary conditions were enforced on the outer edges of the rectangular domain. This solution was then used to calculate the effective diffusion coefficient as a function of x using the mollified triangle function as shown in Eq. (2.44) with and without the correction term. This approach is novel since the size of the closure domain is larger than the averaging volume as opposed to being identical in size. This

allows for the averaging volume to be moved within the closure domain to produce a spatially varying function for the effective diffusivity coefficient as opposed to a single value. The effective diffusion coefficients exhibit oscillatory behavior (Fig. 2.4). However, the magnitude of the fluctuations is much larger for the effective diffusion coefficient calculated using the MVA with the correction term. The source of these fluctuations stems from the accounting for the change in the center of mass as the averaging volume slides across the microscale domain.

Using the effective diffusion coefficients calculated using MVA, Eq. (2.37) was solved on a one-dimensional domain with Dirichlet conditions determined from the DNS solution at each boundary. The resulting concentration profiles are shown (Fig. 2.4) over one period of the domain. Model 2 shows improved accuracy over both Model 0 and 1. Model 1 does not appear to differ noticeably from Model 0 since the contribution of the zero-order porosity term is negligible in homogeneous porous media. The improvement of including the first-order center of mass term in Model 2 is very slight however this provides an example of how the effective diffusivity tensor may possess strong fluctuations in periodic media.

The reason why this correction is successful is directly tied to ensuring that the average concentration only changes linearly throughout each averaging volume. For average concentration profiles with large second derivatives, this approach cannot be guaranteed to give an

Table 2.1: The parameters used for Case 1.

L_x	$1.2 \times 10^{-2}[m]$	Macroscale domain length
L_y	$1.0 \times 10^{-3}[m]$	Macroscale domain width
$c_{A\gamma}(x = 0, y)$	$0 \left[\frac{mol}{m^3}\right]$	Macroscale domain boundary conditions
$c_{A\gamma}(x = L_x, y)$	$1 \left[\frac{mol}{m^3}\right]$	
$\frac{\partial}{\partial y} c_{A\gamma}(x, y = 0)$	$0 \left[\frac{mol}{m^4}\right]$	
$\frac{\partial}{\partial y} c_{A\gamma}(x, y = L_y)$	$0 \left[\frac{mol}{m^4}\right]$	
$\mathcal{D}_{A\gamma}$	$10^{-9} \left[\frac{m^2}{s}\right]$	Microscale diffusion coefficient
ε_γ	0.4	Periodic cell γ -phase porosity
l_κ	$8.36 \times 10^{-4} [m]$	κ -phase square side length
l_p	$1 \times 10^{-3}[m]$	Period length
$r_{0,x}$	$2 \times 10^{-3}[m]$	Averaging volume length
$r_{0,y}$	$1 \times 10^{-3}[m]$	Averaging volume width
ϵ_0	$2.5 \times 10^{-5}[m]$	Mollifying function characteristic length

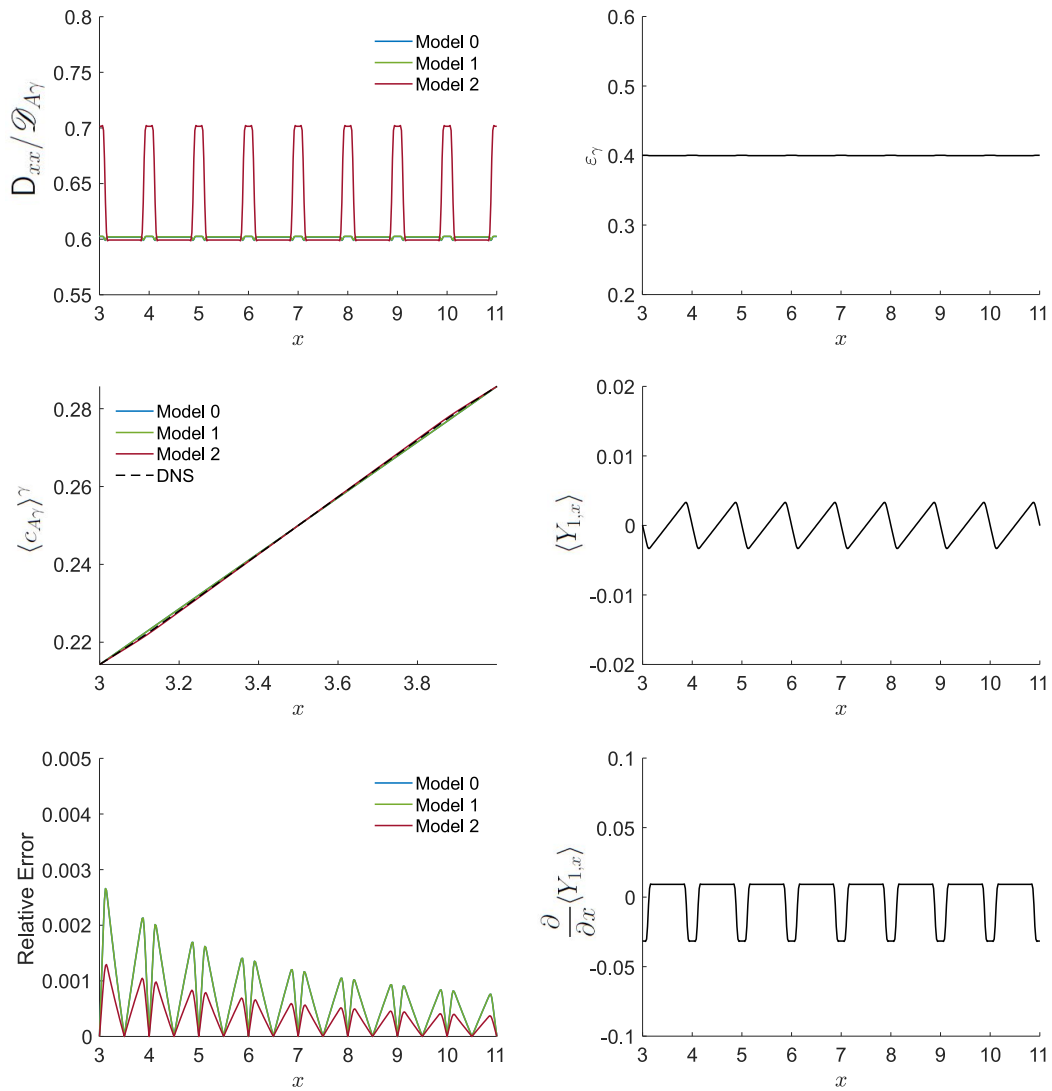


Figure 2.4: The effective diffusivity tensor, averaged concentration profiles, and relative errors of Case 1 (left column, top to bottom) and the porosity, x -component and x -derivative of the first moment vector (right column, top to bottom).

accurate solution. However, assuming that the constraints stated in this analysis are met, it should be clear that additional microscale information may be transferred through the up-scaling process by including the first-order Taylor series expansion term, thus improving the qualitative and quantitative behavior of the calculated macroscale averaged concentration.

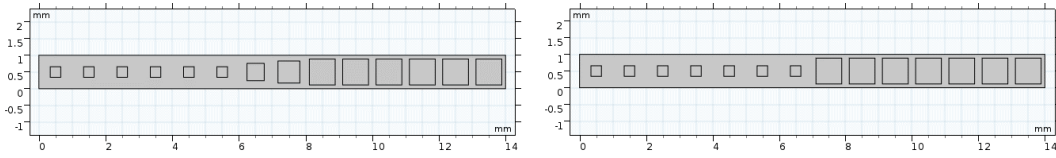


Figure 2.5: The domains for the Case 2: gradually varying porosity (left) and Case 3: discontinuous porosity (right).

2.6 Case 2 and 3: Steady Diffusion in a Spatially Varying Quasi-Periodic Porous Medium

Cases 2 and 3 represent a slightly more complex for upscaling; in these cases the medium is envisioned as being infinitely periodic except for a transition in the porosity occurring in the center of the domain. For Case 2, the change is somewhat gradual as the porosity varies from 0.9 to 0.4 over a four periodic cells (Fig. 2.5, left). For Case 3 the change happens as a discontinuity, where the porosity discontinuously jumps from 0.9 to 0.4 at the center of the domain (Fig. 2.5, right). Because for both Cases 2 and 3 the effective parameters far from the interface are essentially those described for case 1, we focus here specifically on the effective parameters near the interface at $x = L/2$. For both cases, the closure problems (Eqs. 2.39, 2.41, 2.43) are solved using periodic boundary conditions on the outer edges of the rectangular domain. The global constraint $\langle \mathbf{b}_\gamma \rangle = 0$ is added to ensure existence and uniqueness of the closure solution. This solution was then used to calculate the effective diffusion coefficient for each model (Eqs. 2.40, 2.42, 2.44) which was then used to solve the macroscale equation (Eq. 2.37).

2.6.1 Case 2

For each model, the microscale equations used are identical to the constant porosity case; the primary difference arises strictly from the geometry of the domain. For the Case 2, model 0 produces an effective diffusivity tensor that is negative near the interface of the two porous regions (Fig. 2.6, top-left). This results from the inability of model 0 to account for gradients in the geometric properties, and thus it inaccurately captures the average flux across the

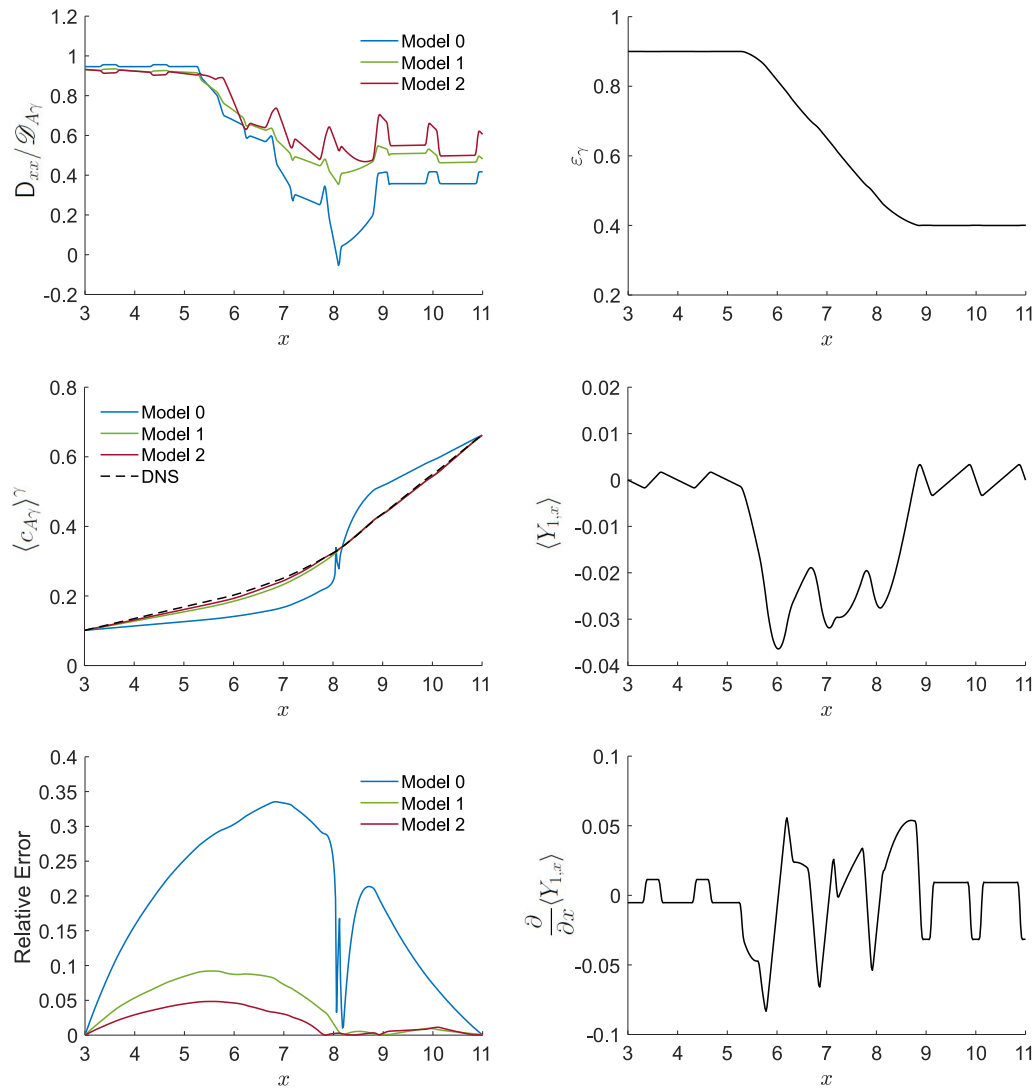


Figure 2.6: The effective diffusivity tensor, averaged concentration profiles, and relative errors of Case 2 (left column, top to bottom) and the porosity, x -component and x -derivative of the first moment vector (right column, top to bottom).

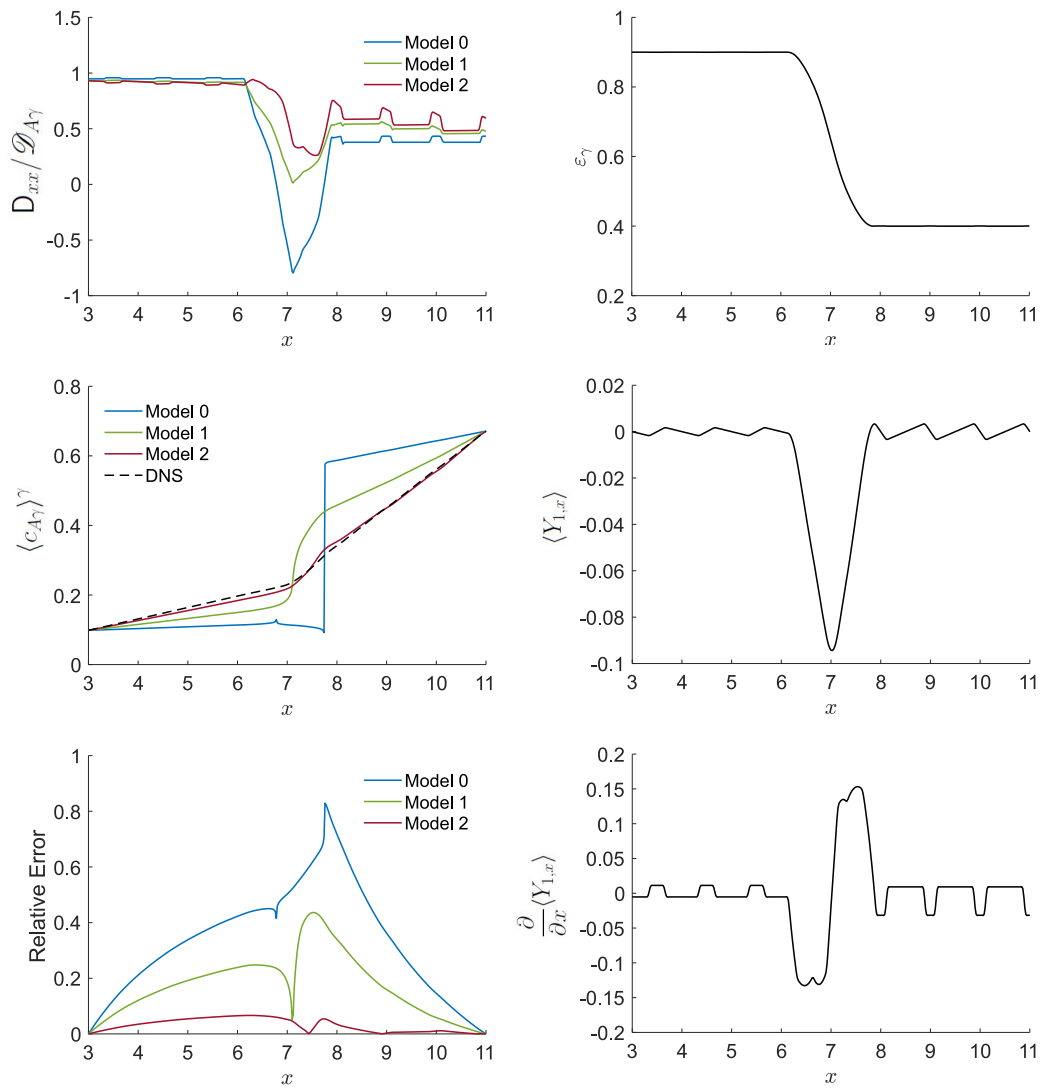


Figure 2.7: The effective diffusivity tensor, averaged concentration profiles, and relative errors of Case 3 (left column, top to bottom) and the porosity, x -component and x -derivative of the first moment vector (right column, top to bottom)

porosity change. Both models 1 and 2 fare better for this case. When the effective diffusivity coefficient from both models 1 and 2 are used to simulate the macroscopic balance equation for this case, they display excellent agreement with averaged concentration that is predicted by averaging the DNS solution directly (Fig. 2.6, middle-left).

Although both models 2 and 3 perform acceptably well, it is clear that including successive terms of the Taylor series for the flux reduces the relative error on average by up to a factor of 10 when comparing Model 0 to Model 2 (Fig. 2.6, bottom-left). In the comparison between models 1 and 2, model 2 shows a smaller improvement, but the relative error by a factor of about 2.

2.6.2 Case 3

The effect of the first moment term is more prominent in Case 3 where the porosity abruptly changes from 0.9 to 0.4 (Fig. 2.7, top-right). Model 0 produces an effective diffusivity tensor with negative values across the porosity jump (Fig. 2.7, top-left). This is a non-physical result that results in the macroscale average diffusion equation to become ill-posed. Models 1 and 2 produce similar diffusivity tensors that only differ significantly in the region of changing porosity. Examining the macroscale average concentration profiles shows that Model 0 completely fails to produce an accurate solution (Fig. 2.7, middle-left). Instead, the problem becomes ill-posed over the porosity jump. The situation is improved for model 1, which remains well-posed, but a large error is incurred due to the porosity interface (Fig. 2.7, bottom-left). Finally, model 2 outperforms as it closely agrees with the averaged DNS solution at all points along the averaged domain. In this case, the first moment significantly reduces the relative error by about a factor of 10 (Fig. 2.7, bottom-right).

In both cases, the use of a proper weighting is required to avoid the introduction of delta functions in the derivative of the averaged quantities as the averaging window passes over the interfaces of the γ - and κ -phases. Our studies have shown that a triangle function mollified with a small bump function smooths the edges and center of the averaging window. This allows for the averages to belong to the space of C^∞ functions. Furthermore, the use of a small bump

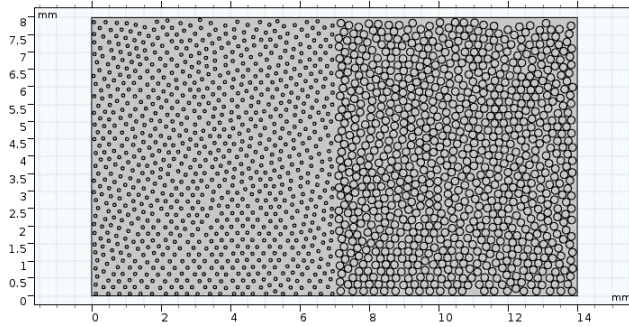


Figure 2.8: Case 4: a disordered porous medium with a 0.5 jump change in porosity.

function largely suppresses any unphysical oscillations in the averaged quantities. We again emphasize the importance of suppressing unphysical oscillations and refer the reader to the Appendix for an example of what occurs when the unphysical oscillations are not suppressed.

2.7 Case 4: Steady Diffusion in a Spatially Varying Disordered Porous Medium

In this section, we examine Case 4, which represents a two-dimensional medium for which there is a jump discontinuity in porosity. The medium is illustrated in (Fig. 2.8). To generate the medium, circles of two different radii ($44.6 \mu m$ and $109 \mu m$) were randomly placed in two distinct subregions of the large-scale domain using an open-source packing algorithm [38]. The resulting porous domain contained a horizontal (x -direction) jump in porosity at an interface along the domain midplane.

As done for the first three cases, the effective diffusion coefficient was predicted from models 0, 1, and 2, and then these effective coefficients were used to predict the average concentration by solving the upscaled equation (2.37) over the domain. For comparison, DNS simulations at the microscale were also conducted, and the average concentration computed by directly applying the averaging operator to the microscale fields. The results from this effort are shown in Fig. 2.10. For clarity, the dimensionality of the results have been reduced by a projection onto the x -axis.

As constructed, the porous domain has a sharp horizontal change in porosity at the center

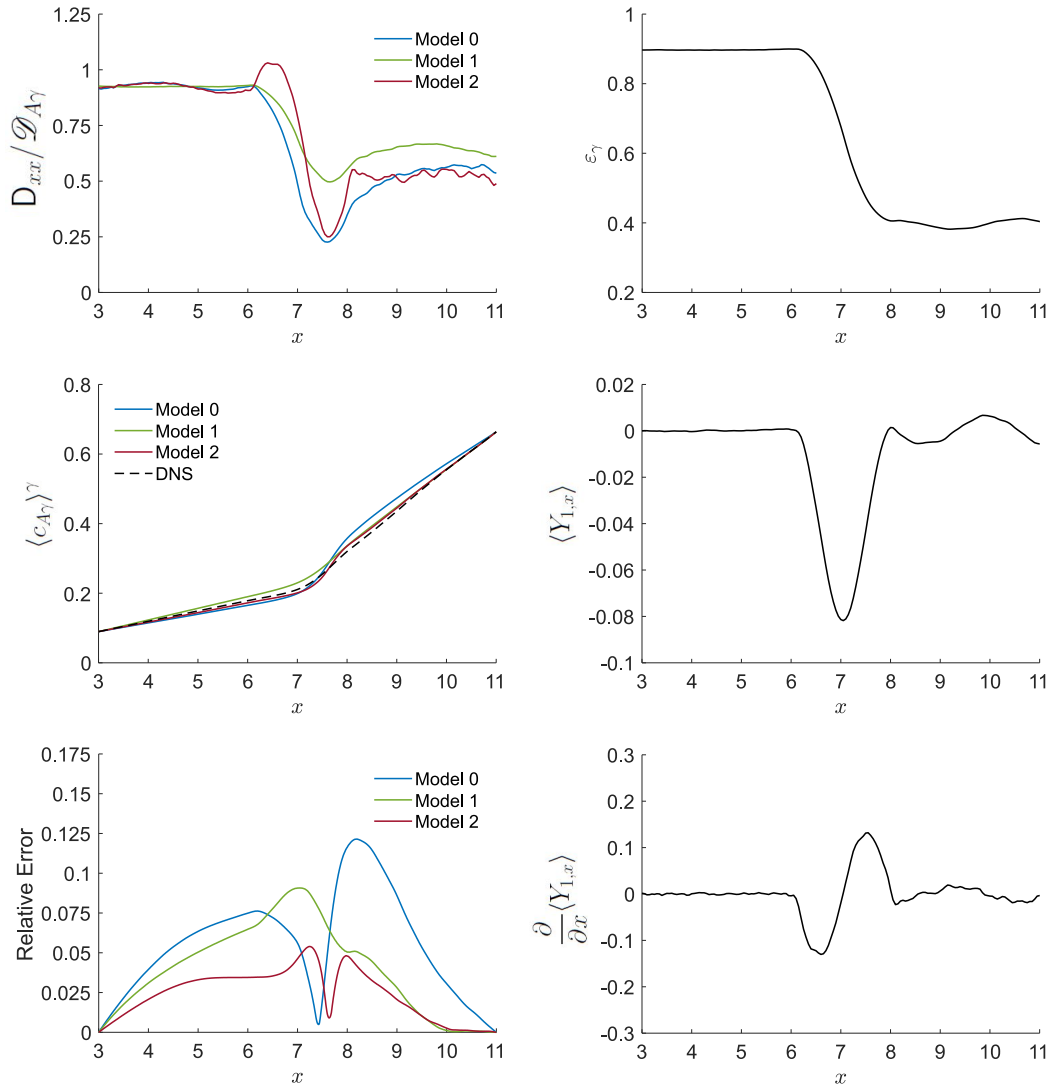


Figure 2.9: The xx -component of the effective diffusivity tensor, averaged concentration profiles, and relative errors of Case 4 (left column, top to bottom) and the porosity, x -component and x -derivative of the first moment vector (right column, top to bottom).

of the domain from $\varepsilon_\gamma = 0.9$ to about $\varepsilon_\gamma = 0.4$. Specific effort was made to assure that the averaging volume was sufficiently large enough so that the average values predicted did not randomly fluctuate significantly in homogeneous parts of the domain (i.e., sufficiently far from the interface). Evidence that the size selected was reasonable can be seen in the plots of the porosity, the x -component of the first moment, and the derivative of the first moment respect to x (Fig. 2.9). As the averaging volume crosses from the high to low porosity regions, the x -derivative of the first moment rapidly changes. This rapid change across the γ - κ interface is due to the most of the γ -phase being located in the highly porous region as the averaging volume transitions to the less porous subdomain. As a result, the first moment vector points in the negative x -direction until the averaging volume fully crosses into the less porous region. This change in the first moment affects both the calculated \mathbf{b}_γ -field and the effective diffusivity tensor. Around the interface, the effective diffusivity coefficient rapidly changes in magnitude. As the averaging volume approaches the interface from the left, the diffusivity tensor experiences a sharp increase in magnitude. Furthermore, as the averaging volume crosses to the less porous region, the diffusivity undergoes a sharp decrease until the averaging volume is sufficiently far away from the interface. These sharp changes in the diffusivity tensor are directly attributable to the derivatives of the first moment vector. Since the first moment represents the γ -phase center of mass, upscaling this information to the macroscale increases the accuracy of the MVA model. This is clearly seen when comparing the concentration profile generated from Model 2 to Models 0 and 1 (Fig. 2.9, middle-left). Model 0 exhibits large deviations from the DNS solution over the entire porous medium. This contrasts to Model 1 which shows good agreement with the DNS solution in the low porosity region, but deviates in the high porosity region and at the γ - κ interface. Model 2 displays increased accuracy in the highly porous region of the material compared to model 1. However, the relative error of model 2 in the low porosity region is comparable to model 1 (Fig. 2.9, bottom-left). Overall, despite the large jump in the porosity, model 2 reduces the relative error by a factor of 3 on average compared to model 0. For discontinuous porosity changes smaller 0.5, the model can be expected to produce better agreement with the DNS solution.

2.8 Convergence of the Taylor Series Approximation for the Average Flux

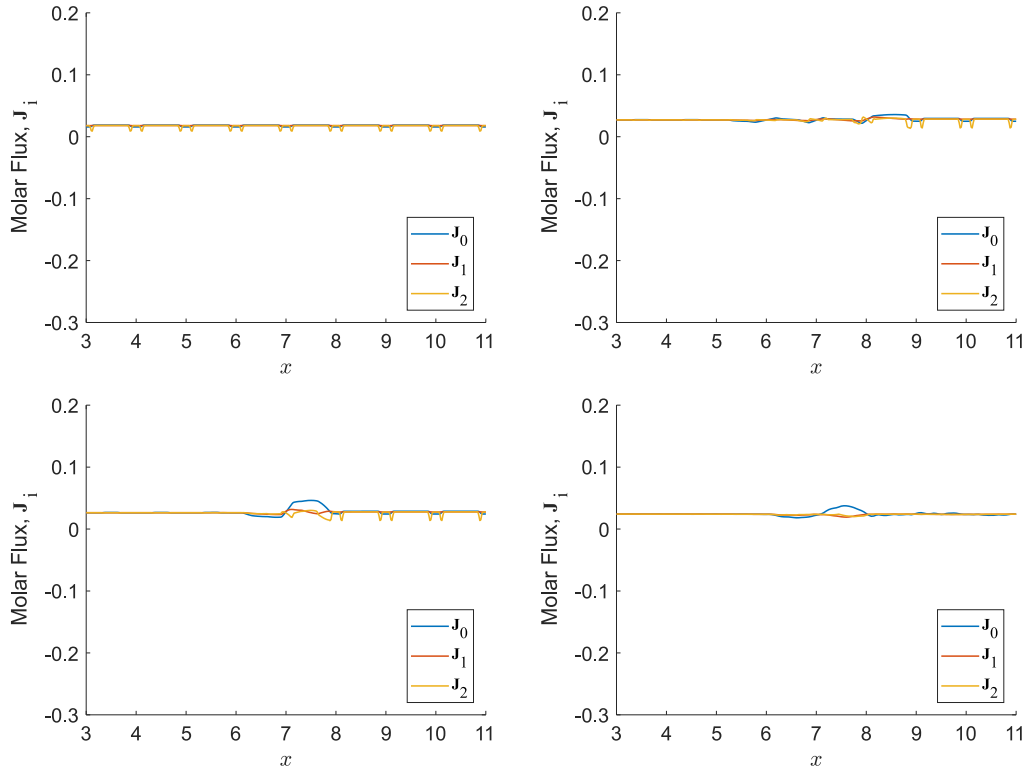


Figure 2.10: The Taylor series average flux approximation for Case 1 (top-left), Case 2 (top-right), Case 3 (bottom-left), and Case 4 (bottom-right).

In this section, we examine how the additional corrections to the diffusion coefficient change the convergence of the flux in the system. Recall that when averaging the microscale diffusion equation, the following nonlocal term containing the integral of the average concentration arises

$$\left\{ \begin{array}{l} \text{nonlocal} \\ \text{term} \end{array} \right\} = \int_{\mathbf{y} \in \mathcal{A}_{\gamma\kappa}(\mathbf{x})} \mathbf{n}_{\gamma\kappa} \langle c_{A\gamma} \rangle^\gamma w(\mathbf{y}) dA(\mathbf{y}) \quad (2.49)$$

Noting that the Taylor series of $\langle c_{A\gamma} \rangle^\gamma |_{\mathbf{x}+\mathbf{y}}$ is written as

$$\langle c_{A\gamma} \rangle^\gamma |_{\mathbf{x}+\mathbf{y}} = \langle c_{A\gamma} \rangle^\gamma |_{\mathbf{x}} + \mathbf{Y}_1 \cdot \nabla \langle c_{A\gamma} \rangle^\gamma |_{\mathbf{x}} + \frac{1}{2} \mathbf{Y}_2 : \nabla \nabla \langle c_{A\gamma} \rangle^\gamma |_{\mathbf{x}} + \dots \quad (2.50)$$

we can substitute this expansion into (Eq. 2.8) to give

$$\int_{\mathbf{y} \in \mathcal{A}_{\gamma\kappa}(\mathbf{x})} \mathbf{n}_{\gamma\kappa} \langle c_{A\gamma} \rangle^\gamma w(\mathbf{y}) dA(\mathbf{y}) = -\nabla \varepsilon_\gamma \langle c_{A\gamma} \rangle^\gamma - \nabla \langle \mathbf{Y}_1 \rangle \cdot \nabla \langle c_{A\gamma} \rangle^\gamma - \nabla \langle \mathbf{Y}_2 \rangle : \nabla \nabla \langle c_{A\gamma} \rangle^\gamma - \dots \quad (2.51)$$

Using this result and Eq. (2.14), the molar flux can be approximated by the following

$$\begin{aligned} \mathbf{J}_\gamma |_{(\mathbf{x}+\mathbf{y})} = \mathcal{D}_{A\gamma} & \left(\varepsilon_\gamma \nabla \langle c_{A\gamma} \rangle^\gamma |_{(\mathbf{x})} - \nabla \langle \mathbf{Y}_1 \rangle \cdot \nabla \langle c_{A\gamma} \rangle^\gamma |_{(\mathbf{x})} \right. \\ & \left. - \frac{1}{2} \nabla \langle \mathbf{Y}_2 \rangle : \nabla \nabla \langle c_{A\gamma} \rangle^\gamma |_{(\mathbf{x})} - \dots + \int_{\mathbf{y} \in \mathcal{A}_{\gamma\kappa}(\mathbf{x})} \mathbf{n}_{\gamma\kappa} \tilde{c}_{A\gamma} w(\mathbf{y}) dA(\mathbf{y}) \right) \end{aligned} \quad (2.52)$$

In this form, the molar flux is presented in a way that the influence of adding successive corrections arising from the Taylor series change the flux. In particular, one can begin to assess whether or not the upscaled flux in this representation even converges or not. Note that if this sequence of partial sums does not converge, it has serious ramifications for the upscaling process. In effect, it would indicate that no truncation of the series would lead to an adequate representation of the average flux in the system. The only other choice would be, then, to explore nonlocal formulations for the flux.

To calculate the partial sums, we solved the microscale PDE (Eq. 2.3) to determine the pointwise concentration. This solution is then directly averaged with the weighting function to create the averaged DNS solution. In this section, a mollified triangle weighting function was used when calculating the averaged quantities. The derivatives of the averaged solution are then used to evaluate the Taylor series terms. As previously, it is assumed that the y -direction is quasi-spatially stationary [?, 32] and that the average concentration only depends on the x -direction. Thus, the Taylor series reduces to a scalar equation for the average flux. The

following three partial sum approximations of the molar flux for the γ -phase are considered

$$\mathbf{J}_0 = \mathcal{D}_{A\gamma} \left(\varepsilon_\gamma \nabla \langle c_{A\gamma} \rangle^\gamma |_{(\mathbf{x})} + \int_{\mathbf{y} \in \mathcal{A}_{\gamma\kappa}(\mathbf{x})} \mathbf{n}_{\gamma\kappa} \tilde{c}_{A\gamma} w(\mathbf{y}) dA(\mathbf{y}) \right) \quad (2.53)$$

$$\mathbf{J}_1 = \mathcal{D}_{A\gamma} \left(\varepsilon_\gamma \nabla \langle c_{A\gamma} \rangle^\gamma |_{(\mathbf{x})} - \nabla \langle \mathbf{Y}_1 \rangle \cdot \nabla \langle c_{A\gamma} \rangle^\gamma |_{(\mathbf{x})} + \int_{\mathbf{y} \in \mathcal{A}_{\gamma\kappa}(\mathbf{x})} \mathbf{n}_{\gamma\kappa} \tilde{c}_{A\gamma} w(\mathbf{y}) dA(\mathbf{y}) \right) \quad (2.54)$$

$$\begin{aligned} \mathbf{J}_2 = \mathcal{D}_{A\gamma} \left(\varepsilon_\gamma \nabla \langle c_{A\gamma} \rangle^\gamma |_{(\mathbf{x})} - \nabla \langle \mathbf{Y}_1 \rangle \cdot \nabla \langle c_{A\gamma} \rangle^\gamma |_{(\mathbf{x})} \right. \\ \left. - \frac{1}{2} \nabla \langle \mathbf{Y}_2 \rangle : \nabla \nabla \langle c_{A\gamma} \rangle^\gamma |_{(\mathbf{x})} + \int_{\mathbf{y} \in \mathcal{A}_{\gamma\kappa}(\mathbf{x})} \mathbf{n}_{\gamma\kappa} \tilde{c}_{A\gamma} w(\mathbf{y}) dA(\mathbf{y}) \right) \end{aligned} \quad (2.55)$$

For the mollified triangle weighting function, the partial sums appear to be converging for all four cases considered in this paper (Fig. 2.10). However, the convergence of the Taylor series is strongly dependent on the particular weighting function used to calculate the averaged quantities. For the mollified boxcar weighting function, we find that the partial sums appear to diverge for the periodic cases considered. Interestingly, the sums converge for the disordered medium of case 4. These results are presented in the appendix.

2.9 Conclusions

The main goal of this study was to derive a MVA model of the transport of mass through a porous material possessing a change in porosity. Doing this required the proper selection of a mollified triangular weighting function and developing a suitable REV for the closure problem. This approach was shown to be suitable for a variety of cases involving both homogeneous and heterogeneous quasi-periodic porous mediums in addition to the case of a disordered porous material. The main findings in the this study are summarized as follows.

1. Incorporating the $\nabla \langle \mathbf{Y}_1 \rangle \cdot \nabla \langle c_{A\gamma} \rangle^\gamma |_{(\mathbf{x})}$ term of the Taylor series expansion results in a significant improvement in the accuracy of mass transport simulations of heterogeneous porous media. In the case of quasi-periodic porous materials, incorporating this additional term decreased the error by a factor of 10. For Case 3, the $\varepsilon_\gamma^{-1} \nabla \varepsilon_\gamma$ term must be

included in the closure problem to ensure that the effective diffusivity tensor is positive definite. However, the accuracy of the MVA model is greatly improved by also including the $-\varepsilon_\gamma^{-1} \nabla \cdot \nabla \otimes \langle y \rangle$ term in the closure problem.

2. Selecting the proper form of the weighting function is paramount in ensuring the convergence of the Taylor series approximation of the average flux of mass through the porous material. Section 2.8 and A illustrate the effect of using a mollified triangle versus a discontinuous and mollified boxcar weighting function. Though the mollified boxcar function more closely represents the uniform weighting function typically used in MVA for homogeneous materials, it fails to accurately approximate the average flux. This results in a non-positive definite effective diffusivity tensor at points where the porosity strongly varies.
3. To ensure the derivatives of the porosity and center of mass term are continuous, the weighting function must be mollified by an infinitely differentiable function. In this study, the bump function was convolved with boxcar and triangle functions so that the resulting averaged properties were sufficiently smooth.
4. The addition of higher order Taylor series terms allows for the utility of MVA to be expanded to porous materials with porosity jumps as large as 0.5. Our experience has shown that for even larger porosity jumps, incorporating the $\nabla \langle \mathbf{Y}_1 \rangle \cdot \nabla \langle c_{A\gamma} \rangle^\gamma |_{(\mathbf{x})}$ term is insufficient to prevent the effective diffusivity tensor from becoming non-positive definite.

This work represents a first step in expanding the applications of MVA to heterogeneous porous materials with extreme changes in porosity. The results of model 2 were compared against an averaged DNS solution and shown to possess a high level of agreement and superior performance compared to the previous reported models 0 and 1. This shows that our approach is indeed performing as expected and is able to accurately approximate the average flux of material across a heterogeneous porous material. Furthermore, the derived model is extremely general and is able to be applied to both quasi-periodic and disordered materials so long as a

”sufficient” REV is selected. Additionally, these results are of course just as applicable to the description of heat transfer through a heterogeneous porous medium. Further investigation is required to expand this model to handle unsteady-state transport.

2.10 Simulation Files and Data

The simulation files and data (geometrical parameters and concentration profile solutions, open-source-format meshes, and MATLAB and COMSOL input files) produced from this study may be found at the following open source electronic archive: <https://ir.library.oregonstate.edu/concern/datasets/9880vw91t>.

Chapter 3: General Conclusions

The main goal of this thesis was to extend the method of volume averaging to the case of heterogeneous porous materials. The manuscript presented addressed several issues in developing such a model for both periodic and disordered porous materials possessing large porosity gradients and investigated the effects of different weighting function on model accuracy. The main benefit of this technique is the ability to implicitly model large porous domains while retaining important microscale information such as the first moment of the phases present within the modeled material. Drawbacks in this approach include the need to still model an REV that may be computationally expensive.

Future work includes applying this model to the description of transport in stratified aquifers, oil reservoirs, and biological tissues. Specific next steps would include adapting the volume averaged equations to include multiphase transport such as the case of extracting oil from sandstone via water flooding. Our current work is admittedly very simplistic, only incorporating diffusion. However, to model oil reservoirs, advective effects must be included in the model. Furthermore, the interactions between oil and water must also be accounted for. Additionally, determining a suitable REV is necessary in order to capture all of the relevant information contained within both the sandstone and the fracture networks that tend to permeate through sandstone. Other applications of this work include the design of materials possessing gradients in porosity such as asymmetric membrane filters. This future work could improve the accuracy of using upscaling methods to model transport phenomena across many length scales.

Bibliography

- [1] S. Torquato, H. Haslach, *Random Heterogeneous Materials: Microstructure and Macroscopic Properties*, ASME International, 2002. doi:10.1115/1.1483342.
URL <https://doi.org/10.1115/1.1483342>
- [2] D. Enke, F. Janowski, W. Schwieger, Porous glasses in the 21st century—a short review, *Microporous and Mesoporous Materials* 60 (1-3) (2003) 19–30. doi:10.1016/s1387-1811(03)00329-9.
URL [https://doi.org/10.1016/s1387-1811\(03\)00329-9](https://doi.org/10.1016/s1387-1811(03)00329-9)
- [3] G. Lewis, Properties of open-cell porous metals and alloys for orthopaedic applications, *Journal of Materials Science: Materials in Medicine* 24 (10) (2013) 2293–2325. doi:10.1007/s10856-013-4998-y.
URL <https://doi.org/10.1007/s10856-013-4998-y>
- [4] M. Rahimi, S. Madaeni, M. Abolhasani, A. A. Alsairafi, CFD and experimental studies of fouling of a microfiltration membrane, *Chemical Engineering and Processing: Process Intensification* 48 (9) (2009) 1405–1413. doi:10.1016/j.cep.2009.07.008.
URL <https://doi.org/10.1016/j.cep.2009.07.008>
- [5] J. Garcia-Aleman, Experimental analysis, modeling, and theoretical design of mcmaster pore-filled nanofiltration membranes, *Journal of Membrane Science* 240 (1-2) (2004) 237–255. doi:10.1016/j.memsci.2004.05.009.
URL <https://doi.org/10.1016/j.memsci.2004.05.009>
- [6] M. K. Hubbert, Darcy’s law and the field equations of the flow of underground fluids, *International Association of Scientific Hydrology. Bulletin* 2 (1) (1957) 23–59. doi:10.1080/02626665709493062.
URL <https://doi.org/10.1080/02626665709493062>
- [7] B. Berkowitz, J. Bear, C. Braester, Continuum models for contaminant transport in fractured porous formations, *Water Resources Research* 24 (8) (1988) 1225–1236. doi:10.1029/wr024i008p01225.
URL <https://doi.org/10.1029/wr024i008p01225>
- [8] J. C. S. Long, J. S. Remer, C. R. Wilson, P. A. Witherspoon, Porous media equivalents for networks of discontinuous fractures, *Water Resources Research* 18 (3) (1982) 645–658. doi:10.1029/wr018i003p00645.
URL <https://doi.org/10.1029/wr018i003p00645>
- [9] G. Barenblatt, I. Zheltov, I. Kochina, Basic concepts in the theory of seepage of homogeneous liquids in fissured rocks [strata], *Journal of Applied Mathematics and Mechanics* 24 (5) (1960) 1286–1303. doi:10.1016/0021-8928(60)90107-6.
URL [https://doi.org/10.1016/0021-8928\(60\)90107-6](https://doi.org/10.1016/0021-8928(60)90107-6)

- [10] J. Warren, P. Root, The behavior of naturally fractured reservoirs, *Society of Petroleum Engineers Journal* 3 (03) (1963) 245–255. doi:10.2118/426-pa.
URL <https://doi.org/10.2118/426-pa>
- [11] K. Pruess, A practical method for modeling fluid and heat flow in fractured porous media, *Society of Petroleum Engineers Journal* 25 (01) (1985) 14–26. doi:10.2118/10509-pa.
URL <https://doi.org/10.2118/10509-pa>
- [12] F. Blaskovich, G. Cain, F. Sonier, D. Waldren, S. Webb, A multicomponent isothermal system for efficient reservoir simulation, in: *Middle East Oil Technical Conference and Exhibition*, Society of Petroleum Engineers, 1983. doi:10.2118/11480-ms.
URL <https://doi.org/10.2118/11480-ms>
- [13] A. Hill, G. Thomas, A new approach for simulating complex fractured reservoirs, in: *Middle East Oil Technical Conference and Exhibition*, Society of Petroleum Engineers, 1985. doi:10.2118/13537-ms.
URL <https://doi.org/10.2118/13537-ms>
- [14] S. Whitaker, *The Method of Volume Averaging*, Springer Netherlands, 1999. doi:10.1007/978-94-017-3389-2.
URL <https://doi.org/10.1007/978-94-017-3389-2>
- [15] E. Sanchez-Palencia, *Nonhomogeneous Media and Vibration Theory*, Vol. 69, Acoustical Society of America (ASA), 1981. doi:10.1121/1.385521.
URL <https://doi.org/10.1121/1.385521>
- [16] L. Tartar, *The General Theory of Homogenization*, Springer Berlin Heidelberg, 2010. doi:10.1007/978-3-642-05195-1.
URL <https://doi.org/10.1007/978-3-642-05195-1>
- [17] H. Lonsdale, The growth of membrane technology, *Journal of Membrane Science* 10 (2-3) (1982) 81–181. doi:10.1016/s0376-7388(00)81408-8.
URL [https://doi.org/10.1016/s0376-7388\(00\)81408-8](https://doi.org/10.1016/s0376-7388(00)81408-8)
- [18] G. Daufin, J.-P. Escudier, H. Carrère, S. Bérot, L. Fillaudeau, M. Decloux, Recent and emerging applications of membrane processes in the food and dairy industry, *Food and Bioproducts Processing* 79 (2) (2001) 89–102. doi:10.1205/096030801750286131.
URL <https://doi.org/10.1205/096030801750286131>
- [19] T. Burnouf, M. Radosevich, Nanofiltration of plasma-derived biopharmaceutical products, *Haemophilia* 9 (1) (2003) 24–37. doi:10.1046/j.1365-2516.2003.00701.x.
URL <https://doi.org/10.1046/j.1365-2516.2003.00701.x>
- [20] K. Ferrand, A. Abdelouas, B. Grambow, Water diffusion in the simulated french nuclear waste glass SON 68 contacting silica rich solutions: Experimental and modeling, *Journal of Nuclear Materials* 355 (1-3) (2006) 54–67. doi:10.1016/j.jnucmat.2006.04.005.
URL <https://doi.org/10.1016/j.jnucmat.2006.04.005>
- [21] E. A. Sudicky, R. W. Gillham, E. O. Frind, Experimental investigation of solute transport in stratified porous media: 1. the nonreactive case, *Water Resources Research* 21 (7)

- (1985) 1035–1041. doi:10.1029/wr021i007p01035.
URL <https://doi.org/10.1029/wr021i007p01035>
- [22] C. Zhangxin, Large-scale averaging analysis of single phase flow in fractured reservoirs, *SIAM Journal on Applied Mathematics* 54 (3) (1994) 641–659. doi:10.1137/s0036139992235202.
URL <https://doi.org/10.1137/s0036139992235202>
- [23] I. L. Novak, P. Kraikivski, B. M. Slepchenko, Diffusion in cytoplasm: Effects of excluded volume due to internal membranes and cytoskeletal structures, *Biophysical Journal* 97 (3) (2009) 758–767. doi:10.1016/j.bpj.2009.05.036.
URL <https://doi.org/10.1016/j.bpj.2009.05.036>
- [24] I. Griffiths, A. Kumar, P. Stewart, Designing asymmetric multilayered membrane filters with improved performance, *Journal of Membrane Science* 511 (2016) 108–118. doi:10.1016/j.memsci.2016.02.028.
URL <https://doi.org/10.1016/j.memsci.2016.02.028>
- [25] M. P. Dalwadi, I. M. Griffiths, M. Bruna, Understanding how porosity gradients can make a better filter using homogenization theory, *Proceedings of the Royal Society A: Mathematical, Physical and Engineering Science* 471 (2182) (2015) 20150464. doi:10.1098/rspa.2015.0464.
URL <https://doi.org/10.1098/rspa.2015.0464>
- [26] D.-W. Chung, P. R. Shearing, N. P. Brandon, S. J. Harris, R. E. Garcia, Particle size polydispersity in li-ion batteries, *Journal of the Electrochemical Society* 161 (3) (2014) A422–A430. doi:10.1149/2.097403jes.
URL <https://doi.org/10.1149/2.097403jes>
- [27] S. Granet, P. Fabrie, P. Lemonnier, M. Quintard, A single-phase flow simulation of fractured reservoir using a discrete representation of fractures, in: *ECMOR VI - 6th European Conference on the Mathematics of Oil Recovery*, EAGE Publications BV, 1998. doi:10.3997/2214-4609.201406633.
URL <https://doi.org/10.3997/2214-4609.201406633>
- [28] F. J. Valdés-Parada, J. Alvarez-Ramírez, A volume averaging approach for asymmetric diffusion in porous media, *The Journal of Chemical Physics* 134 (20) (2011) 204709. doi:10.1063/1.3594549.
URL <https://doi.org/10.1063/1.3594549>
- [29] M. Bruna, S. J. Chapman, Diffusion in spatially varying porous media, *SIAM Journal on Applied Mathematics* 75 (4) (2015) 1648–1674. doi:10.1137/141001834.
URL <https://doi.org/10.1137/141001834>
- [30] Y. Davit, M. Quintard, Technical notes on volume averaging in porous media i: How to choose a spatial averaging operator for periodic and quasiperiodic structures, *Transport in Porous Media* 119 (3) (2017) 555–584. doi:10.1007/s11242-017-0899-8.
URL <https://doi.org/10.1007/s11242-017-0899-8>

- [31] C. C. Seepersad, J. K. Allen, D. L. McDowell, F. Mistree, Multifunctional topology design of cellular material structures, *Journal of Mechanical Design* 130 (3) (2008) 031404. doi:10.1115/1.2829876.
URL <https://doi.org/10.1115/1.2829876>
- [32] B. D. Wood, F. J. Valdés-Parada, Volume averaging: Local and nonlocal closures using a green's function approach, *Advances in Water Resources* 51 (2013) 139–167. doi:10.1016/j.advwatres.2012.06.008.
URL <https://doi.org/10.1016/j.advwatres.2012.06.008>
- [33] W. Gray, P. Lee, On the theorems for local volume averaging of multiphase systems, *International Journal of Multiphase Flow* 3 (4) (1977) 333–340. doi:10.1016/0301-9322(77)90013-1.
URL [https://doi.org/10.1016/0301-9322\(77\)90013-1](https://doi.org/10.1016/0301-9322(77)90013-1)
- [34] J. H. Cushman, Proofs of the volume averaging theorems for multiphase flow, *Advances in Water Resources* 5 (4) (1982) 248–253. doi:10.1016/0309-1708(82)90009-4.
URL [https://doi.org/10.1016/0309-1708\(82\)90009-4](https://doi.org/10.1016/0309-1708(82)90009-4)
- [35] W. G. Gray, A. Leijnse, R. L. Kolar, C. A. Blain, *Mathematical tools for changing scale in the analysis of physical systems*, CRC Press, 1993.
- [36] C. T. Miller, F. J. Valdés-Parada, S. Ostvar, B. D. Wood, A priori parameter estimation for the thermodynamically constrained averaging theory: Species transport in a saturated porous medium, *Transport in Porous Media* 122 (3) (2018) 611–632. doi:10.1007/s11242-018-1010-9.
URL <https://doi.org/10.1007/s11242-018-1010-9>
- [37] J. Bear, Y. Bachmat, Mathematical statement of a transport problem, in: *Introduction to Modeling of Transport Phenomena in Porous Media*, Springer Netherlands, 1990, pp. 263–286. doi:10.1007/978-94-009-1926-6_3.
URL https://doi.org/10.1007/978-94-009-1926-6_3
- [38] B. Fornberg, N. Flyer, Fast generation of 2-d node distributions for mesh-free PDE discretizations, *Computers & Mathematics with Applications* 69 (7) (2015) 531–544. doi:10.1016/j.camwa.2015.01.009.
URL <https://doi.org/10.1016/j.camwa.2015.01.009>
- [39] B. Wood, S. Apte, J. Liburdy, R. Ziazi, X. He, J. Finn, V. Patil, A comparison of measured and modeled velocity fields for a laminar flow in a porous medium, *Advances in Water Resources* 85 (2015) 45–63. doi:10.1016/j.advwatres.2015.08.013.
URL <https://doi.org/10.1016/j.advwatres.2015.08.013>
- [40] Procedure for estimation and reporting of uncertainty due to discretization in CFD applications, *Journal of Fluids Engineering* 130 (7) (2008) 078001. doi:10.1115/1.2960953.
URL <https://doi.org/10.1115/1.2960953>
- [41] P. J. Roache, Conservatism of the grid convergence index in finite volume computations on steady-state fluid flow and heat transfer, *Journal of Fluids Engineering* 125 (4) (2003)

731. doi:10.1115/1.1588692.
URL <https://doi.org/10.1115/1.1588692>

APPENDICES

Appendix A: Approximating the Average Molar Flux

We depict the importance of choosing a proper weighting function in this section. Commonly, a uniform weighting function is used for VAT. However, this approach encounters issues as the averaging window crosses γ - κ interfaces. For example, taking the derivative of the porosity will generate delta functions when using a uniform weighting function. Case 1 is solved using the discontinuous boxcar function (Fig. A.1, top-right). The Taylor series is shown to diverge at the γ - κ interfaces (Fig. A.1, top-left). As a result, the effective diffusivity tensor possesses negative values at the interfaces for model 2 (Fig. A.1, bottom-left). However, the effective diffusivity is well-behaved for models 0 and 1 and are in fact identical. Because of the divergent nature of the molar flux approximation, model 2 becomes ill-posed and performs worse than models 0 and 1 (Fig. A.1, bottom-right).

Additionally, here we will also show that mollifying the uniform weighting function is not sufficient to obtain accurate effective parameters for heterogeneous porous media. For this portion of the study, a two-unit cell wide boxcar function is mollified with a bump function that is 20% the width of a single unit cell (Fig. A.2, top-right). The resulting weighting function possesses continuous derivatives of all orders (Fig. A.2). The Taylor series approximation of the flux was calculated using the DNS solution for Case 1 and 2. The goal of this exercise is to qualitatively observe whether the Taylor series solution displays divergent behavior (Fig. A.2). The partial sums using the first three terms of the Taylor series for both the case of constant porosity and gradual porosity change appear to not be converging where the averaging volume cross the γ - κ interfaces. This effect is more pronounced in low porous regions. Checking the partial sums of the first, second, and third Taylor series terms clearly shows that the flux is not being approximated well using this weighting function for Cases 1 and 2 (Fig. A.2, left column). Furthermore, compared to the mollified triangle weighting function, the mollified boxcar function predicted fluxes are an order of magnitude higher in the γ -phase regions

between the κ -phase. Interestingly, the Taylor series appears to be converging for Case 4, however the convergence is slower in the low porosity region of the porous material (Fig. A.2, bottom-right).

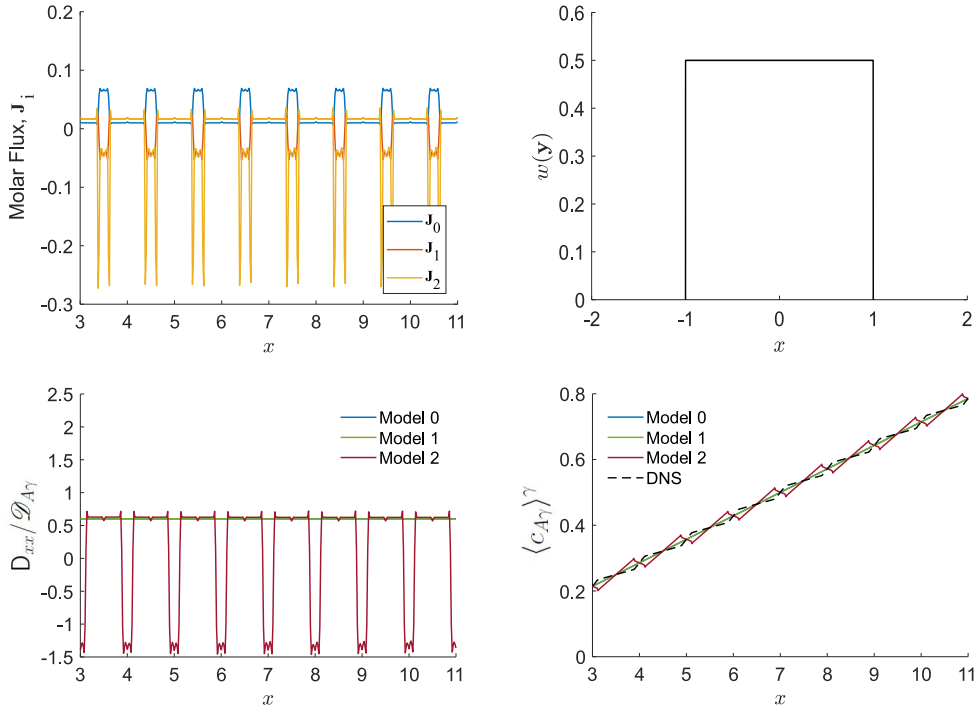


Figure A.1: The boxcar function (top-right) and the Taylor series approximated average flux for the Case 1 (top-left), the effective diffusivity coefficient (bottom-left) and the concentration profile (bottom-right) using a boxcar weighting function.

For the Case 1, models 0 and 1 produce a non-negative effective diffusion coefficient, however model 2 gives a diffusion coefficient that is negative whenever the averaging window crosses a γ - κ interface (Fig. A.3, top-row). Similar problems exist for Case 2. However, the change in porosity causes the diffusion coefficients of all models are negative in the low porosity regions (Fig. A.3, middle-row). As a result, none of the models are valid using the mollified boxcar function for Case 2.

Because the approximation of the flux is not convergent, the effective diffusion coefficient is unable to be accurately calculated using the mollified boxcar function which causes model 2 to fail in both porosity cases. Though this line of reasoning does not fully explain why

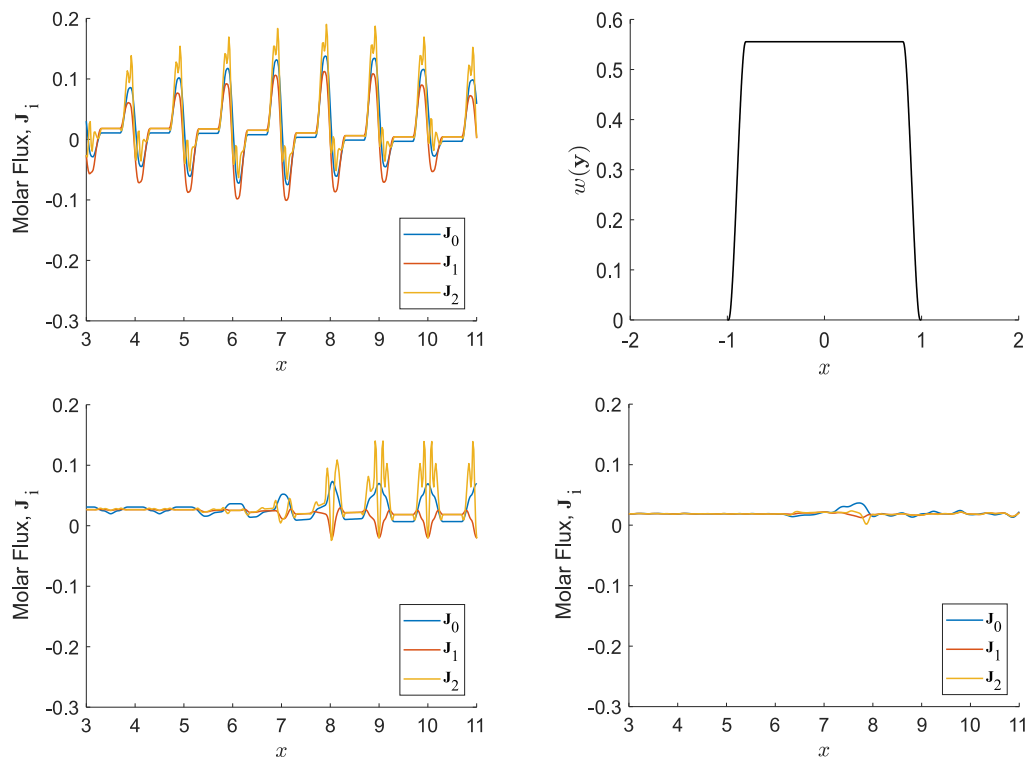


Figure A.2: The mollified boxcar function (top-right) and the Taylor series approximated average flux for the Case 1 (top-left), Case 2 (bottom-left) and Case 4 (bottom-right) using a mollified boxcar weighting function.

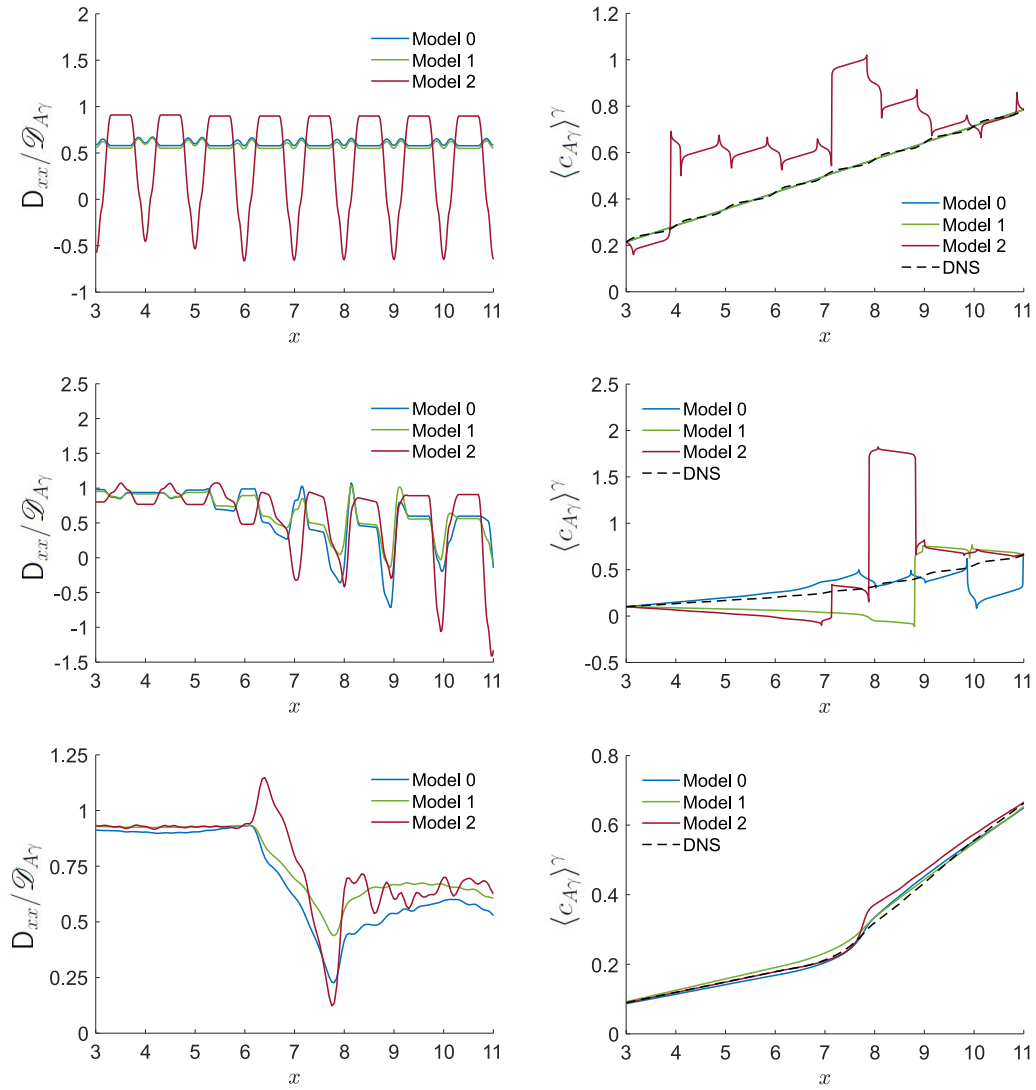


Figure A.3: The effective diffusion coefficient (left column) and average concentration profile (right column) for Case 1, Case 2, and Case 4 (top to bottom row) for the mollified boxcar function.

only model 2 fails for the case of constant porosity. However, if we look at the formula for the effective diffusion coefficient (Eq. 2.44), it is seen that the term containing the first-order correction is neglected in models 0 and 1. We have observed that the first-order correction is particularly prone to over-correcting the model for low porosities when an improper weighting function is used. Because of this, the magnitude of the first-order correction will determine whether the effective diffusion coefficient will be positive for all points in space. For the cases where this is not true, the calculated effective diffusion coefficient will be negative in regions near the γ - κ interfaces. Since models 0 and 1 ignore the contributions of the first-order term, both are guaranteed to never produce a negative diffusion coefficient for domains with constant porosity. This is of course not true when the porosity varies as seen in Fig. A.2.

All of this contrasts to the disordered porous media case in which the Taylor Series does appear to be convergent (Fig. A.2, bottom). However, the rate of convergence is slow in the low porosity region which mirrors the degraded accuracy of model 2 in this region. This suggests that while the mollified boxcar function is admissible as a weighting function for MVA, the produced results will suffer in terms of accuracy compared to the mollified triangle weighting function.

Appendix B: Analysis of Source Terms

In general, the sum of all source terms for a steady-state diffusion on a compact domain with periodic boundaries must have a spatial average equal to zero; if it is not equal to zero, the source would generate new mass within the volume for all time, and no steady state would exist. To start, we examine the sources in model 1

$$\nabla^2 \mathbf{b}_\gamma = \varepsilon_\gamma^{-1} \nabla \varepsilon_\gamma \quad (\text{B.1})$$

$$B.C. 1 \quad -\mathbf{n}_{\gamma\kappa} \cdot \nabla \mathbf{b}_\gamma = \mathbf{n}_{\gamma\kappa}, \quad \text{for } \mathbf{x} \in \mathcal{A}_{\gamma\kappa} \quad (\text{B.2})$$

$$B.C. 2 \quad \mathbf{b}_\gamma(\mathbf{r} + \mathbf{l}) = \mathbf{b}_\gamma(\mathbf{r}), \quad \text{for } \mathbf{x} \in \mathcal{A}_{\gamma\mathbf{e}} \quad (\text{B.3})$$

$$(\text{B.4})$$

Integrating both sides of Eq. (B.1), we find

$$\int_{\mathbf{r} \in V_\gamma} \nabla^2 \mathbf{b}_\gamma dV(\mathbf{r}) = \int_{\mathbf{r} \in V_\gamma} \varepsilon_\gamma^{-1} \nabla \varepsilon_\gamma dV(\mathbf{r}) \quad (\text{B.5})$$

Now, using the divergence theorem and the periodicity of the flux, we find

$$\int_{\mathbf{r} \in \mathcal{A}_{\gamma\kappa}(\mathbf{x})} \mathbf{n}_{\gamma\kappa} \cdot \nabla \mathbf{b}_\gamma dV(\mathbf{r}) = \int_{\mathbf{r} \in \mathcal{A}_{\gamma\kappa}(\mathbf{x})} \mathbf{n}_{\gamma\kappa} dA(\mathbf{r}) \quad (\text{B.6})$$

This result represents the integrated volume source (i.e., the source given on the right-hand side of Eq. (B.1))

The second source term is the boundary source represented by Eq. (B.2). Integrating both sides of the expression given by *B.C. 2* over the phase interface, we find

$$\int_{\mathbf{r} \in \mathcal{A}_{\gamma\kappa}(\mathbf{x})} \mathbf{n}_{\gamma\kappa} \cdot \nabla \mathbf{b}_\gamma dA(\mathbf{r}) = - \int_{\mathbf{r} \in \mathcal{A}_{\gamma\kappa}(\mathbf{x})} \mathbf{n}_{\gamma\kappa} dA(\mathbf{r}) \quad (\text{B.7})$$

From this result, it is clear that the two source terms for model 1 have equal average values, but with opposite signs. Thus, the net source term in the problem has zero average.

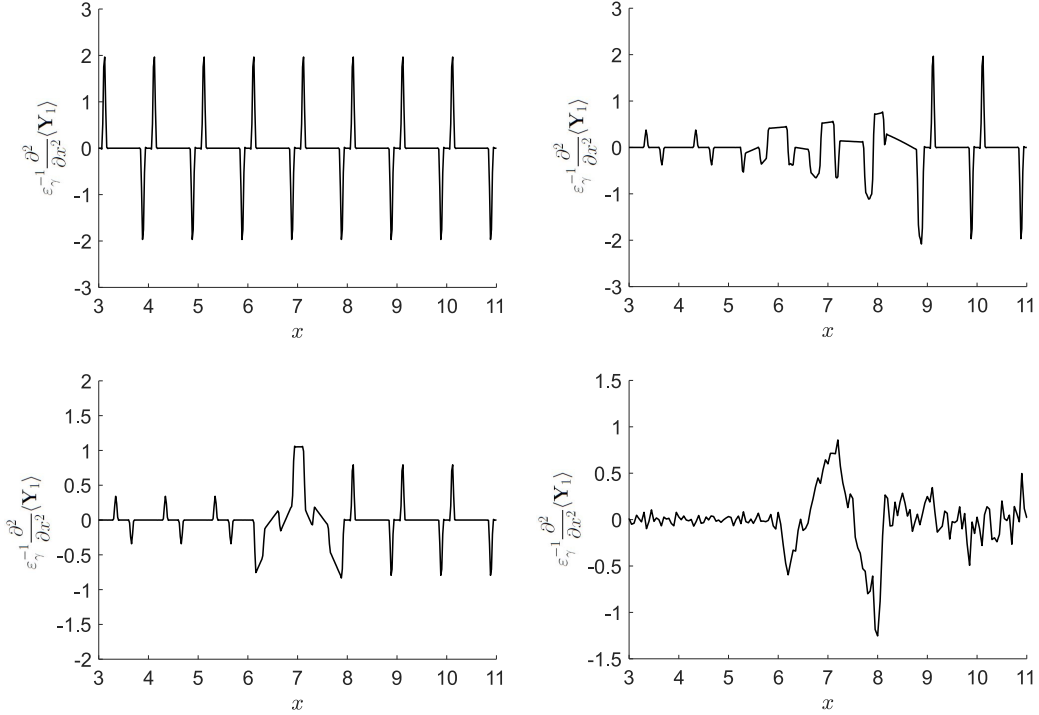


Figure B.1: The first moment source term for Case 1 (top-left), Case 2 (top-right), Case 3 (bottom-left), and Case 4 (bottom-right).

For the additional source associated with model 2 (the term $-\varepsilon_\gamma^{-1} \nabla \cdot \nabla \otimes \langle \mathbf{Y}_1 \rangle$), the analytical analysis is complicated by the fact that it depends upon the value of the first moment of the medium. This moment is coupled strongly to the geometry, and it is not easily computed analytically except for the simplest cases.

Regardless, we can compute the value of the additional source term numerically. Noting that each of the cases examined have variations of the moments only in the horizontal (x -) direction, it is easy to verify that the source term in this case reduces to the consideration of

$$-\varepsilon_\gamma^{-1} \partial^2 \langle \mathbf{Y}_1 \rangle / \partial x^2.$$

In Figure B.1, we have plotted the value of $-\varepsilon_\gamma^{-1} \partial^2 \langle \mathbf{Y}_1 \rangle / \partial x^2$ as a function of x . The requirement that the source term have an average of zero was assessed by integrating these functions as follows. Let $M_0 = \max[\text{abs}(\varepsilon_\gamma^{-1} \partial^2 \langle \mathbf{Y}_1 \rangle / \partial x^2)]$

$$\epsilon_{source} = \int_x \frac{1}{M_0} \varepsilon_\gamma^{-1} \frac{\partial^2 \langle \mathbf{Y}_1 \rangle}{\partial x^2} \quad (\text{B.8})$$

The results were as follows: Case 1, $\epsilon_{source} = 1.24 \times 10^{-7}$; Case 2, $\epsilon_{source} = -0.005$, Case 3, $\epsilon_{source} = -0.003$; Case 4, $\epsilon_{source} = -0.005$. These values are sufficiently small that we may assume that the criterion for zero average source is met to within numerical error.

Appendix C: Convergence Analysis

For both macroscale and microscale solutions, the grid convergence index, GCI_G , and global convergence order, P_G are reported in Tables C.1-C.4 for the DNS, closure problem, and upscaled equation solutions [39, 40, 41]. The GCI_G provides a percent relative error estimate of the calculated solutions based upon Richardson's extrapolation. For each solution the estimated error is below 3% with typical values on the order of thousandths of a percent.

Table C.1: The global convergence order, P_G , global GCI and average element size, \bar{h} for the DNS solution, closure problem, and upscaled equations for Case 1

	P_G	GCI_G [%]	\bar{h} [m]
$c_{A\gamma}$	2.89	1.34×10^{-3}	4.88×10^{-5}
$\mathbf{b}_{\gamma,0}$	2.84	5.13×10^{-1}	9.98×10^{-6}
$\mathbf{b}_{\gamma,1}$	2.80	2.35×10^0	9.98×10^{-6}
$\mathbf{b}_{\gamma,2}$	2.84	2.26×10^0	4.81×10^{-5}
$\langle c_{A\gamma} \rangle_0^\gamma$	2.91	1.39×10^{-7}	1.00×10^{-5}
$\langle c_{A\gamma} \rangle_1^\gamma$	2.90	1.38×10^{-7}	1.00×10^{-5}
$\langle c_{A\gamma} \rangle_2^\gamma$	2.69	1.16×10^{-6}	1.00×10^{-5}

Table C.2: The global convergence order, P_G , global GCI and average element size, \bar{h} for the DNS solution, closure problem, and upscaled equations for Case 2

	P_G	GCI_G [%]	\bar{h} [m]
$c_{A\gamma}$	1.88	2.10×10^{-3}	1.96×10^{-5}
$\mathbf{b}_{\gamma,0}$	1.68	1.66×10^{-2}	4.86×10^{-5}
$\mathbf{b}_{\gamma,1}$	1.40	4.51×10^{-2}	4.86×10^{-5}
$\mathbf{b}_{\gamma,2}$	2.53	4.23×10^{-3}	3.20×10^{-5}
$\langle c_{A\gamma} \rangle_0^\gamma$	N/A	N/A	N/A
$\langle c_{A\gamma} \rangle_1^\gamma$	2.65	5.30×10^{-5}	1.00×10^{-5}
$\langle c_{A\gamma} \rangle_2^\gamma$	2.96	8.07×10^{-8}	1.00×10^{-5}

Table C.3: The global convergence order, P_G , global GCI and average element size, \bar{h} for the DNS solution, closure problem, and upscaled equations for Case 3

	P_G	GCI_G [%]	\bar{h} [m]
$c_{A\gamma}$	2.48	2.51×10^{-3}	1.96×10^{-5}
$\mathbf{b}_{\gamma,0}$	1.59	3.31×10^{-3}	1.97×10^{-5}
$\mathbf{b}_{\gamma,1}$	1.45	2.15×10^{-2}	1.97×10^{-5}
$\mathbf{b}_{\gamma,2}$	2.56	1.12×10^{-5}	2.44×10^{-5}
$\langle c_{A\gamma} \rangle_0^\gamma$	N/A	N/A	N/A
$\langle c_{A\gamma} \rangle_1^\gamma$	2.97	1.25×10^{-10}	1.00×10^{-5}
$\langle c_{A\gamma} \rangle_2^\gamma$	2.85	7.92×10^{-13}	1.00×10^{-5}

Table C.4: The global convergence order, P_G , global GCI and average element size, \bar{h} for the DNS solution, closure problem, and upscaled equations for Case 4.

	P_G	GCI_G [%]	\bar{h} [m]
$c_{A\gamma}$	2.55	2.54×10^{-1}	3.90×10^{-8}
$\mathbf{b}_{\gamma,0}$	1.63	5.84×10^{-1}	4.00×10^{-8}
$\mathbf{b}_{\gamma,1}$	1.54	1.25×10^{-1}	4.00×10^{-8}
$\mathbf{b}_{\gamma,2}$	1.75	3.38×10^{-1}	4.00×10^{-8}
$\langle c_{A\gamma} \rangle_0^\gamma$	1.86	2.19×10^{-4}	5.00×10^{-5}
$\langle c_{A\gamma} \rangle_1^\gamma$	1.88	1.32×10^{-4}	5.00×10^{-5}
$\langle c_{A\gamma} \rangle_2^\gamma$	1.95	7.04×10^{-4}	5.00×10^{-5}

Nomenclature

Abbreviations

DNS Direct numerical solution

MVA The method of volume averaging

REV Representative elementary volume

Greek Letters

ϵ_0 The half-width of the mollifying function

γ The fluid phase

κ The solid phase

ϵ_γ The volume fraction of the γ -phase within the averaging volume

Roman Letters

$\langle c_{A\gamma} \rangle^\gamma$ The macroscale average concentration of species A in the γ -phase, $\frac{mol}{m^3}$

$\langle c_{A\gamma} \rangle_i^\gamma$ The macroscale average concentration of the model *excluding* the i^{th} Taylor series term, $\frac{mol}{m^3}$

$\langle \mathbf{Y}_1 \rangle$ The center of mass of the γ -phase within the averaging volume, m

$\mathcal{A}_e(\mathbf{x})$ The outer surface of the averaging volume centered at \mathbf{x} , m^2

$\mathcal{A}_{\gamma e}(\mathbf{x})$ The exterior surface of the averaging volume belonging to the γ -phase, m

$\mathcal{A}_{\gamma\kappa}$ Interfacial area between fluid γ -phase and solid κ -phase, m^2

$\mathcal{A}_{\kappa e}(\mathbf{x})$ The exterior surface of the averaging volume belonging to the κ -phase, m

$\mathcal{D}_{A\gamma}$	The microscale diffusion coefficient for species A in the γ -phase, $\frac{m^2}{s}$
$\mathcal{F}_\gamma(\mathbf{r})$	A function for the concentration profile along $\mathcal{A}_{\gamma e}(\mathbf{x})$ in the γ -phase, $\frac{mol}{m^3}$
$\mathcal{V}(\mathbf{x})$	Averaging volume centered at \mathbf{x} , m^3
$\mathcal{V}_\gamma(\mathbf{x})$	The γ -phase volume contained within an averaging volume centered at \mathbf{x} , m^3
$\mathcal{V}_\kappa(\mathbf{x})$	The κ -phase volume contained within an averaging volume centered at \mathbf{x} , m^3
\mathbf{D}_{eff}	Effective diffusivity for the steady-state diffusion model, $\frac{m^2}{s}$
\mathbf{I}	Unit tensor
$\tilde{c}_{A\gamma}$	The deviation of the macroscale average concentration from the microscale concentration of species A in the γ -phase, $\frac{mol}{m^3}$
$c_{A\gamma}$	The microscale concentration of species A in the γ -phase, $\frac{mol}{m^3}$
I_γ	A function indicating the location of the γ -phase within the microscale domain
$w(\mathbf{y})$	The function used to weight the contributions of the properties being averaged within the averaging volume
\mathbf{b}_γ	A vector field that relates $\nabla\langle c_{A\gamma} \rangle$ to $c_{\tilde{A}\gamma}$, m
\mathbf{J}_γ	The macroscale molar flux, $\frac{mol}{m^2 \cdot s}$
\mathbf{J}_i	The molar flux including the i^{th} Taylor series term, $\frac{mol}{m^2 \cdot s}$
$\mathbf{n}_{\gamma\kappa}$	The unit normal vector pointing from the γ - to the κ -phase, m
\mathbf{y}	The set of vectors pointing to every point of the γ -phase relative to the centroid of the averaging volume, m

